

ERRATA

THE CORRECTIONS BELOW ARE *INCLUDED*
IN THIS REVISED VERSION OF THE DOCUMENT

DCA02MA001
NOVEMBER 12, 2001
BELLE HARBOR, NEW YORK

**GROUP CHAIRMAN'S AIRCRAFT
PERFORMANCE STUDY ADDENDUM #2**

- Page 46 has been changed to refer to the “ultimate load design envelope” and the legend in Figures 3.5.4(a) and 3.5.4(b) (pages 47 and 48) have been updated to remove references to limit load for the A, B, C, and D Corner points. (October 2004)

NATIONAL TRANSPORTATION SAFETY BOARD

Office of Research and Engineering
Washington, D.C. 20594

August 16, 2004

Aircraft Performance

Group Chairman's Aircraft Performance Study Addendum #2 by Daniel R. Bower, PhD and John O'Callaghan

ABSTRACT

This second *Addendum* to the *Aircraft Performance Study*¹ uses the Flight Data Recorder (FDR) data latency information described in the first *Addendum* to the *Study*,² together with FDR and Cockpit Voice Recorder information, to define the range of values of the airplane's sideslip and rudder angles at the moment the vertical tail separated from the airplane. These sideslip and rudder angle ranges are then used to define the range of the aerodynamic loads on the vertical tail at the moment of separation. The load range definition accounts for the deformation of the airplane structure under load, as well as the non-linear behavior of the loads resulting from aerodynamic flow separation over the tail in the sideslip and rudder angle ranges of interest, as determined from wind tunnel data, Computational Fluid Dynamics (CFD), and Finite Element Analysis (FEA) calculations. In the vertical tail structural coordinate system, the estimated tail shear load at the time of the right rear attachment lug fracture ranges from $-353,000$ to $-436,000 \pm 5\%$ Newtons (N), the tail root bending moment ranges from $1,580,000$ to $1,840,000 \pm 5\%$ Newton-meters (N*m), and the torsion moment ranges from $18,600$ to $48,100 \pm 5\%$ N*m.

¹ See Reference 1.

² See Reference 2.

1. INTRODUCTION

1.1. Accident Identification

Location: Belle Harbor, New York
 Date: November 12, 2001
 Time: 09:17 AM Eastern Standard Time (EST)
 Flight: American Airlines Flight 587
 Aircraft: Airbus A300B4-605R, Registration N14053
 NTSB#: DCA02MA001

1.2 Aircraft Performance Group Members

Chairman: John O'Callaghan
 National Resource Specialist - Aircraft Performance
 National Transportation Safety Board (NTSB)
 490 L'Enfant Plaza E, SW
 Washington, DC 20594

Members: Daniel Bower, PhD
 Senior Aerospace Engineer
 NTSB

Dominique Buisson
 Senior Expert – Flight Operations
 Engineering – Systems and Integration Tests Center
 Airbus
 1 Rond Point Maurice Bellonte
 31707 Blagnac Cedex, France

Captain Jerry Mumfrey
 F100/A300 Technical Pilot, Flight Operations Technical
 American Airlines
 4601 Highway 360
 Fort Worth, Texas 76155

Steven O'Neal
 Flight Test Engineer
 Federal Aviation Administration (FAA)
 Seattle Aircraft Certification Office, ANM-160S
 1601 Lind Avenue, S.W.
 Renton, Washington 98055-4056

Yann Torres
 Investigator – Engineering Department
 Bureau Enquetes - Accidents (BEA)
 Bâtiment 153 - Aéroport du Bourget
 93352 Le Bourget Cedex, France

1.3 Accident Summary

On November 12, 2001, at approximately 9:17 AM Eastern Daylight Time (EDT), American Airlines flight 587 (AAL587), an Airbus Industrie A300-600, was destroyed when it crashed into a residential area of Belle Harbor, New York, shortly after takeoff from runway 31L at John F. Kennedy International Airport (JFK), Jamaica, New York. Before impact, the vertical stabilizer, rudder, and left and right engines departed the airplane. The 2 pilots, 7 flight attendants, 251 passengers, and 5 persons on the ground were killed. Visual meteorological conditions prevailed and an instrument flight rules flight plan had been filed for the flight destined for Santo Domingo, Dominican Republic. The scheduled passenger flight was conducted under 14 *Code of Federal Regulations* (CFR) Part 121.

1.4. Uncertainty in the Sideslip Angle (β)

Addendum 1 to the *Aircraft Performance Study* describes how the time associated with the recorded DFDR Euler angles can be delayed in time relative to other DFDR parameters, which introduces errors into computations that use both the delayed Euler angles and other, non-delayed parameters as inputs. Figure 3 of *Addendum 1* shows the effects a 250 millisecond delay in the recorded heading angle and a 125 millisecond delay in the recorded pitch and roll angles have on the computed sideslip angle (β); at the time of the “loud bang” recorded on the Cockpit Voice Recorder (CVR), β increases by about 2°. This increased β will increase the loads at rupture. There is therefore some uncertainty in the loads at rupture, as the loads depend on β , and β depends on the value of data latencies in the recorded data.

The 250 ms and 125 ms delays in heading, pitch and roll used in *Addendum 1* lie in the middle of the possible range of delays for these parameters. To determine the possible range in loads on the tail at rupture, the effect of the full range of data latencies must be considered. An additional source of uncertainty in β (and consequently the loads) lies in the methods used to compute β from the recorded data, which require interpolation between recorded Euler angle data points, and estimates of wind speed and direction.

Section 3.1 of this *Addendum* describes the uncertainties in the β calculation associated with different combinations of the full range of recording latencies and β calculation methods, and presents the range of possible β as a function of time accounting for these uncertainties. Section 3.2 presents an estimate of the β range at the time of tail separation.

1.5. Non-Linear Effects on Vertical Tail Loads

The A300-600 Linear Loads Module (LLM) provided by Airbus is a set of data and equations that describe the shear, bending moment, and torsion moments on the vertical tail³ as a function of β , rudder deflection (δ_r), dynamic pressure, and other aircraft state parameters. The LLM is based on wind tunnel measurements of the tail loads. The LLM approximates the corrected wind tunnel data using simple, linear assumptions for the effects of β and δ_r ; i.e., the load on the tail varies proportionally with δ_r and β . This is a good approximation of the real behavior of the loads over a large range of β , where the airflow

³ See Section 1.6 for the definition of these loads.

over the tail is well behaved; however, as with all lifting surfaces, as β continues to increase, the flow will start to separate and the load produced by the tail will no longer increase linearly with incidence angle (β in this case). At some point the flow will be completely separated and the tail will be aerodynamically stalled, and further increases in β will further deviate from linear behavior. Wind tunnel data for an A330-200 airplane⁴ received from Airbus indicated that at the sideslip angles of interest in the accident, flow separation was producing a departure from the linear behavior inherent in the LLM.

The A330 wind tunnel data included individual pressure measurements at numerous pressure taps on the vertical tail. The pressure taps were placed at 5 spanwise locations. At each spanwise location, several taps were placed on each side of the fin in the chordwise direction, corresponding to a streamwise measurement when the aircraft is at a lower angle of attack. Airbus provided pressure data at a range of airplane sideslip angles from -10° to $+9^\circ$, and at several rudder angles⁵.

Airbus also provided an integrated calculation of the shear force coefficient, bending moment coefficient, and torsion moment coefficient (see Section 1.6 for the definition of these load coefficients). The integration in the chordwise direction was done using the raw pressure distributions, fit with an Akima⁶ cubic spline. In the spanwise direction, since there were measurements at only 5 spanwise locations, an elliptical load distribution was fit to the data to provide the integrated force and coefficients. In all wind tunnel tests, the boundary layer transition was fixed at 10% of the chord.

Data was provided at a range of sideslip angles, and several rudder deflection angles. Of interest in the investigation was the data at 7.4° , 10.4° and 14.8° of rudder deflection, since the most probable point of failure in the accident occurred at a rudder deflection between 10° and 11° . The integrated coefficient data, as shown in Figure 1.5.1 for rudder deflection of 10.4° , shows a predominantly linear behavior over the lower ranges of sideslip angle (β) for all coefficients. However, all coefficients show a definite reduction from linear behavior at $\beta = 10^\circ$.

⁴ See Section 2.1 for an explanation of why wind tunnel data for the A330 airplane is used in this *Addendum*.

⁵ The sign convention for rudder deflection is positive to the left. A positive sideslip angle is nose left of the wind.

⁶ See Reference 7.

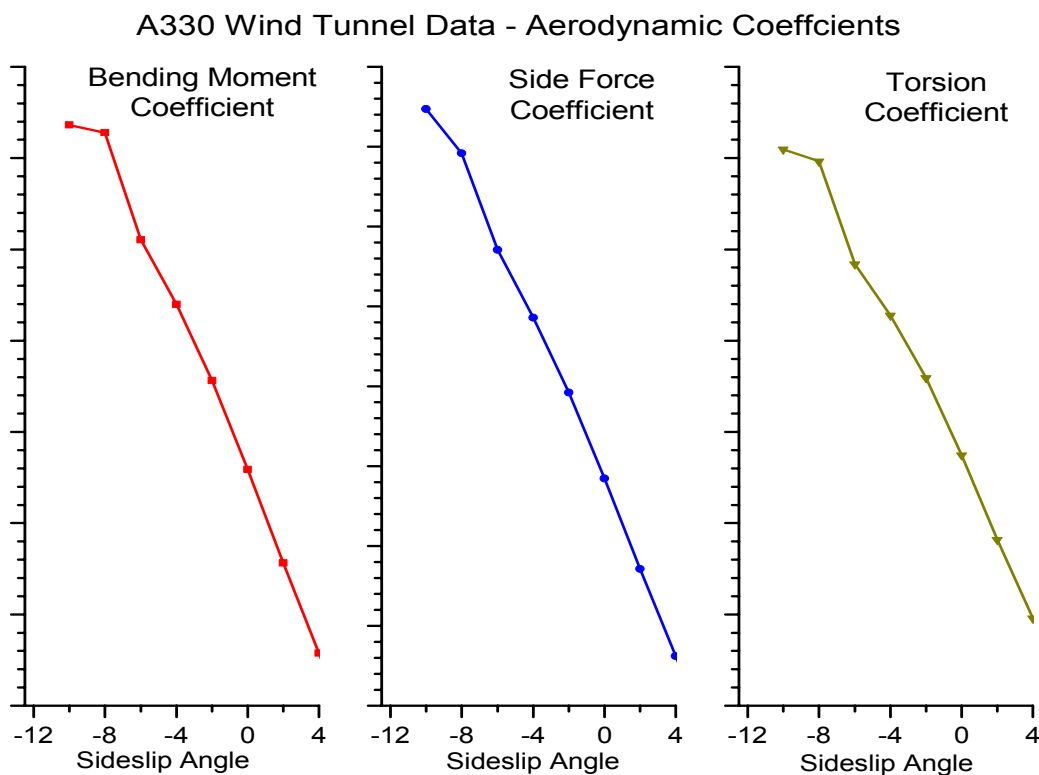


Figure 1.5.1. A330 Wind Tunnel Data Coefficients. Data source: Reference 3, pp. 28-30.

Uncertainty is present in the measured data due to experimentation and instrumentation inaccuracies. However, the trends evident, most notably in the bending moment coefficient, are larger than the experimental error in the data, and are indicative of flow features at the test conditions and model orientation. The reduction of the coefficients from linear behavior was indicative of flow separation on the fin. To examine the nature of this flow phenomenon, further study was required.

The wind tunnel data cannot be used to calculate the flight loads on the accident aircraft directly, since the accident occurred at a much higher flight Reynold's number⁷, and slightly lower Mach number⁸ than the test conditions. Additionally, the wind tunnel model is a rigid A330 configuration, and does not deform with the aerodynamic loads, as actually happens with a full-scale aircraft in flight. This also required further study to evaluate the loads on the A300 at the accident conditions. Additionally, the effect of the nonlinearities at the sideslip angles experienced at the point of structural failure needed to be better understood.

A further examination of the pressure distributions at two of the spanwise locations where data was taken is shown in Figure 1.5.2. Eta, or η , is defined as $\eta = z/b_v$, where z is the distance from the tail root in the airplane axis system (see Figure 2.5.1), and b_v is the tail span (≈ 8.3 m). The chordwise location is measured by x/c , where x is the distance from the

⁷ The Reynold's number (Re) measures the ratio of inertial to viscous forces in the airflow, and increases with the scale of the airplane. In otherwise similar conditions, separation will occur earlier at lower Re.

⁸ Compressibility effects at higher Mach number tend to make flow separation occur earlier than at lower Mach number.

leading edge, and c is the local chord length. Pressures are measured in terms of the pressure coefficient:

$$C_p = \frac{P - P_\infty}{\bar{q}_\infty} \quad [1]$$

Where P is the measured pressure, P_∞ is the freestream static pressure, and \bar{q}_∞ is the freestream dynamic pressure. In Figure 1.5.2, data is shown near the base of the fin, at $\eta = 0.382$, and near the tip, at $\eta = 0.80$ for a sideslip angle of -10° and rudder deflection of -10.4° . The onset of flow separation is observed in the reduction of the pressure peak in the $\eta = 0.80$ data and “flattening” of the pressure profile on the low-pressure side of the fin, typical of the onset of flow separation. As seen in this data, the onset of separation first appears with increased sideslip angle at the outer (i.e. toward the tip) portion of the fin, as expected with the swept configuration of the fin.

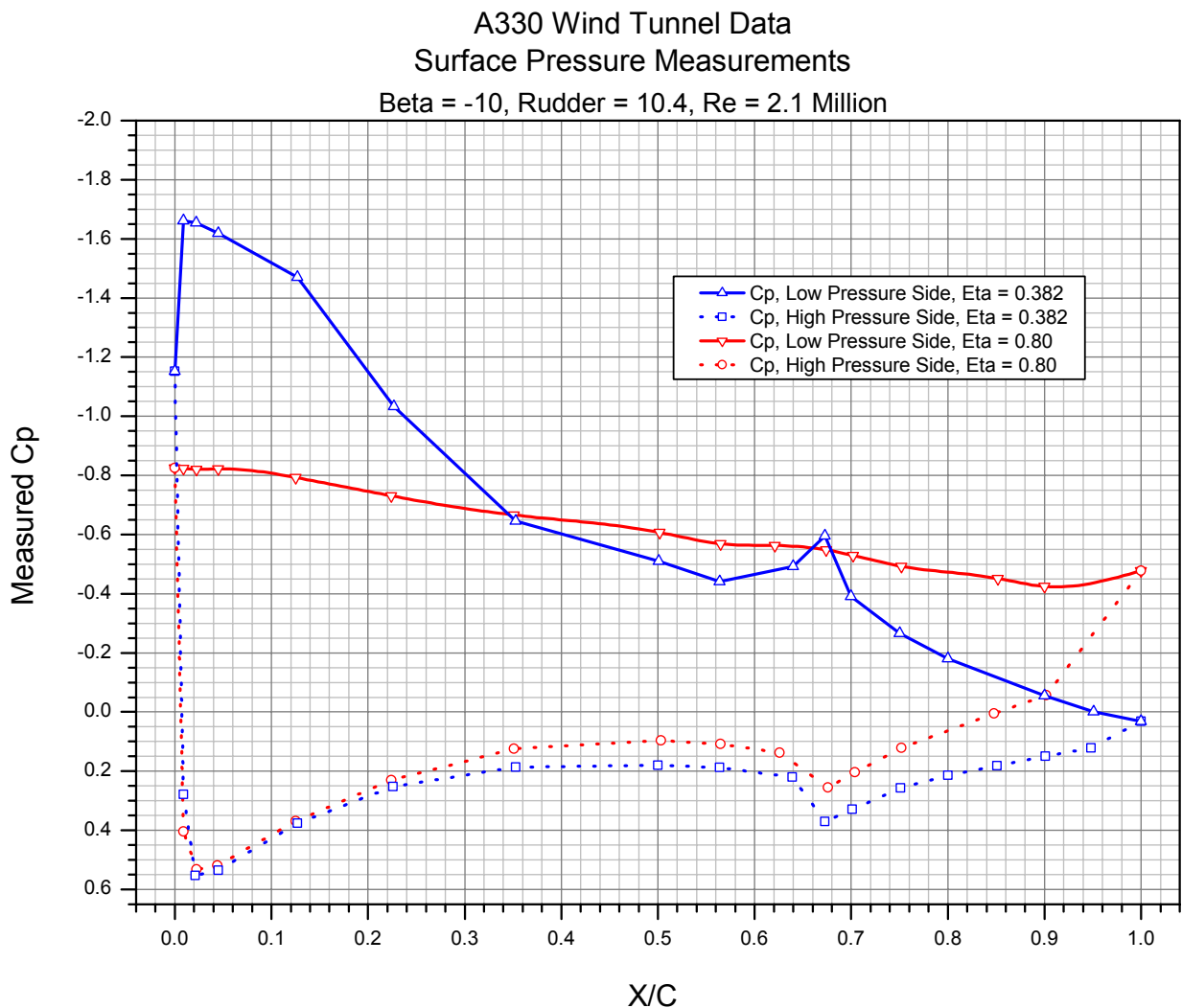


Figure 1.5.2. Chordwise pressure distributions at $\eta = 0.382$ and 0.80 . Data source: Reference 3, pp. 14-16.

To examine the nature of the non-linearities in the wind tunnel data, and to most accurately determine the aerodynamic loads on the accident aircraft vertical tail at flight conditions, the Safety Board requested that Airbus perform a Computational Fluid Dynamic (CFD) study. Whereas the flow over the fin is what is generating the aerodynamic loads, it was recognized that the flow over the tail is greatly influenced by the upstream airflow over the entire aircraft. A computation of the airflow over the entire aircraft was therefore needed to most accurately calculate the aerodynamic loads on the fin. Airbus possessed the three dimensional computational mesh of the A300-600 required to perform this type of study.

Airbus performed the calculations using the CFD code TAU, which has a demonstrated capability⁹ to execute a large scale, three dimensional complex flow computation in the flight regime of interest, and is used extensively by Airbus. The TAU flow solver code was developed by the Deutschen Zentrum für Luft- und Raumfahrt (DLR, German Aerospace Center) to solve the Reynolds averaged Navier-Stokes equations in three dimensions. TAU calculates a steady solution to the equations by marching in time from the initial conditions using an explicit Runge-Kutta time integration. Solutions are marched forward in time, influenced by the boundaries (with aircraft and far field), until changes in the solution are negligible. For the flow regimes examined, a 1-equation Spalart-Allmaras turbulence model was used, and is considered within the aerodynamics community to be a good balance between accuracy and computational complexity for external aerodynamics.

The computational grid used by Airbus for this study was a hybrid grid, consisting of a structured grid near the surface of the aircraft to capture the boundary layer, and near other areas of large flow gradients. An unstructured grid was created to fill the rest of the computational volume away from the structured grid. Additionally, a grid adaptation scheme was used that would automatically adapt the grid according to the given solution, and refine the grid in areas where needed to increase accuracy. The TAU flow solver, grid generation tools, and grid adaptation software is considered by Airbus to be a state-of-the-art system for analyzing these types of flows, and is currently used by Airbus in aircraft configuration and design, generation of aerodynamic data, and prediction of component aero loading.

To determine the effects of aeroelasticity, and compare the aerodynamic loads for a flexible and rigid structure, Airbus forwarded the rigid aerodynamic loads calculated for the (full scale) A300-600 at accident conditions into a coupled NASTRAN/Trunckenbrodt method finite element model (FEM) of the A300-600 vertical tail, which calculated the structural deformation of the fin and rudder surface¹⁰. The deformation of the fuselage was assumed to be linearly dependent upon sideslip angle. The Trunckenbrodt method was used to calculate the changes in the aerodynamic loading on the deformed surface, which is then run through the finite element model. This method is repeated until the deformation of the surface is balanced with the load calculated by the Trunckenbrodt method. The deformed geometry was then forwarded into the grid generation software, and a TAU CFD run was executed for the deformed geometry.

Section 2 describes methods for estimating the actual load behavior based on the information available from the wind tunnel data and the CFD studies performed by Airbus. Section 3.5 presents the results of using these methods to estimate the range of loads at tail separation.

⁹ See Reference 4.

¹⁰ The Airbus CFD / FEM study is described in detail in Reference 8.

1.6. Measuring Loads: Shear, Bending Moment, and Torsion Moment Coefficients

The aerodynamic forces acting on a body are primarily a function of the size and shape of the body, the orientation of the body to the flow, and the dynamic pressure of the flow itself¹¹. At a given orientation, the forces on a body vary proportionally with the body size and the dynamic pressure of the flow; this property allows the forces for bodies of similar shapes to be determined for any scale or dynamic pressure by means of non-dimensional coefficients. For the A300-600 vertical tail loads, the coefficients of interest are those of the shear force, tail root bending moment, and torsion moment. The definitions of these load coefficients are as follows:

$$C_Y = \frac{Y}{\bar{q}S} \quad [2a]$$

$$C_B = \frac{B}{\bar{q}Sb_v} \quad [2b]$$

$$C_T = \frac{T}{\bar{q}S\bar{c}_v} \quad [2c]$$

Where Y is the shear load, B is the bending moment about the vertical tail root chord, and T is the torsion moment about a vertical axis normal to the root chord (see Section 2.5). \bar{q} is the dynamic pressure, S is the vertical tail area (45.2 m²), b_v is the vertical tail span (8.3 m), and \bar{c}_v is the vertical mean aerodynamic chord (5.788 m). The loads are usually expressed in one of two coordinate systems: airplane coordinates and vertical tail structural coordinates. In this Addendum, the loads are computed from CFD and wind tunnel data by integrating pressures over the tail surface; this integration is most easily done in the airplane coordinate system, and therefore the load coefficient results presented in this *Addendum* are in that system. However, the design loads of the tail are expressed in the structural coordinate system, and so the loads are transformed into this system so that comparisons to the tail's design limit loads can be made more easily. The axis systems and transformation matrices are presented in more detail in Section 2.5.

¹¹ Other factors, such as Reynold's number and Mach number, also affect the forces acting on a body. The load coefficients described by Equations [2] will therefore in general be a function of these factors, as well as the orientation of the body to the flow.

2. METHOD

2.1. Wind Tunnel and CFD Data Sources for Computing Vertical Tail Loads

The tail loads presented in the *Aircraft Performance Study* are based on the Airbus LLM. An early objective of the Aircraft Performance Group (ACPG) was to validate the LLM against the original wind tunnel data upon which it is based, particularly at the high β achieved in the accident. However, the original A300 wind tunnel data was lost during the transfer of wind tunnel testing responsibilities between different Airbus sites in Germany, and a copy of portions of the data was not discovered until late in the accident investigation (September, 2003). In the meantime, wind tunnel data for an A330-200 airplane¹² was available and indicated that at about $\beta = 8^\circ$ and rudder (δ_r) = -10° , the bending and torsion moment load behavior with β start to deviate from the linear behavior assumed in the LLM as a result of flow separation on the vertical tail, and from the tip in particular (see Figure 2.1.1). As a result, the ACPG concluded that the LLM, which assumes linear load behavior with β at all values of β , may overestimate the actual loads in the non-linear region ($\beta > 8^\circ$), and that the non-linear effects must be accounted for when determining the value of the loads at tail separation. The A330-200 wind tunnel data set that indicated the onset of non-linear behavior at $\beta = 8^\circ$ was limited by model geometry and mounting constraints to $-10^\circ \leq \beta \leq 9^\circ$, but the accident tail must have separated at a β between 11.3° and 14.1° (see Section 3.2)¹³. Consequently, the A330 wind tunnel data does not cover the β range in question, and loads in this range must either be extrapolated from the wind tunnel data or computed by some other means.

In addition to the β range difficulty, other effects which introduce differences between the aerodynamic characteristics of the airplane at wind tunnel and flight conditions must be considered when computing the loads on the (real) airplane at the time of tail separation. These include:

Reynold's Number (Re) Effect: The Re measures the ratio of inertial to viscous forces in the airflow, and increases with the scale of the airplane. In otherwise similar conditions, separation will occur earlier (at lower β) as Re decreases.

Mach Number (M) Effect: Compressibility effects at higher M tend to make separation occur earlier than at lower M.

Flexibility Effects: The wind tunnel models are very rigid compared to the structure of the real airplane. Consequently, the deformation of the real aerodynamic surface under load, and the consequent change in the load, are not duplicated in the wind tunnel.

Geometry Differences: The A330 and A300 tails are similar, but not identical. Furthermore, details in the geometry, such as the gap between the vertical tail and the rudder, may have an affect on the airflow that is difficult to model or reproduce.

¹² The A330-200 and A300-600 aft fuselage and vertical tail geometries, while not identical, are very similar. Consequently, the aerodynamic performance of the A300-600 tail can be estimated by integrating the non-dimensional pressure coefficient distributions corresponding to the A330-200 tail over the A300-600 tail geometry.

¹³ Because the airplane is symmetrical about its longitudinal axis, the aerodynamic characteristics at negative β and positive δ_r values are equal and opposite to the characteristics at equivalent positive β and negative δ_r values. This property is used throughout the work described in this *Addendum* to take maximum advantage of the range of β and δ_r angles tested in the wind tunnel.

Localized Flow Effects: Wind tunnel models included a mechanism (a trip) to trigger the boundary layer to transition from laminar flow to turbulent. In-flight, transition occurs naturally, and location is dependent upon flow conditions, surface configuration, roughness, etc.

In order to determine the aerodynamic characteristics of the tail at higher β (and in particular the nature and extent of flow separation), and to account for the differences in these characteristics between wind tunnel and flight conditions, the NTSB requested that Airbus conduct a Computational Fluid Dynamics study of the A300-600 and A330-200 vertical tails. The CFD code and methods used are described in Section 1.5.

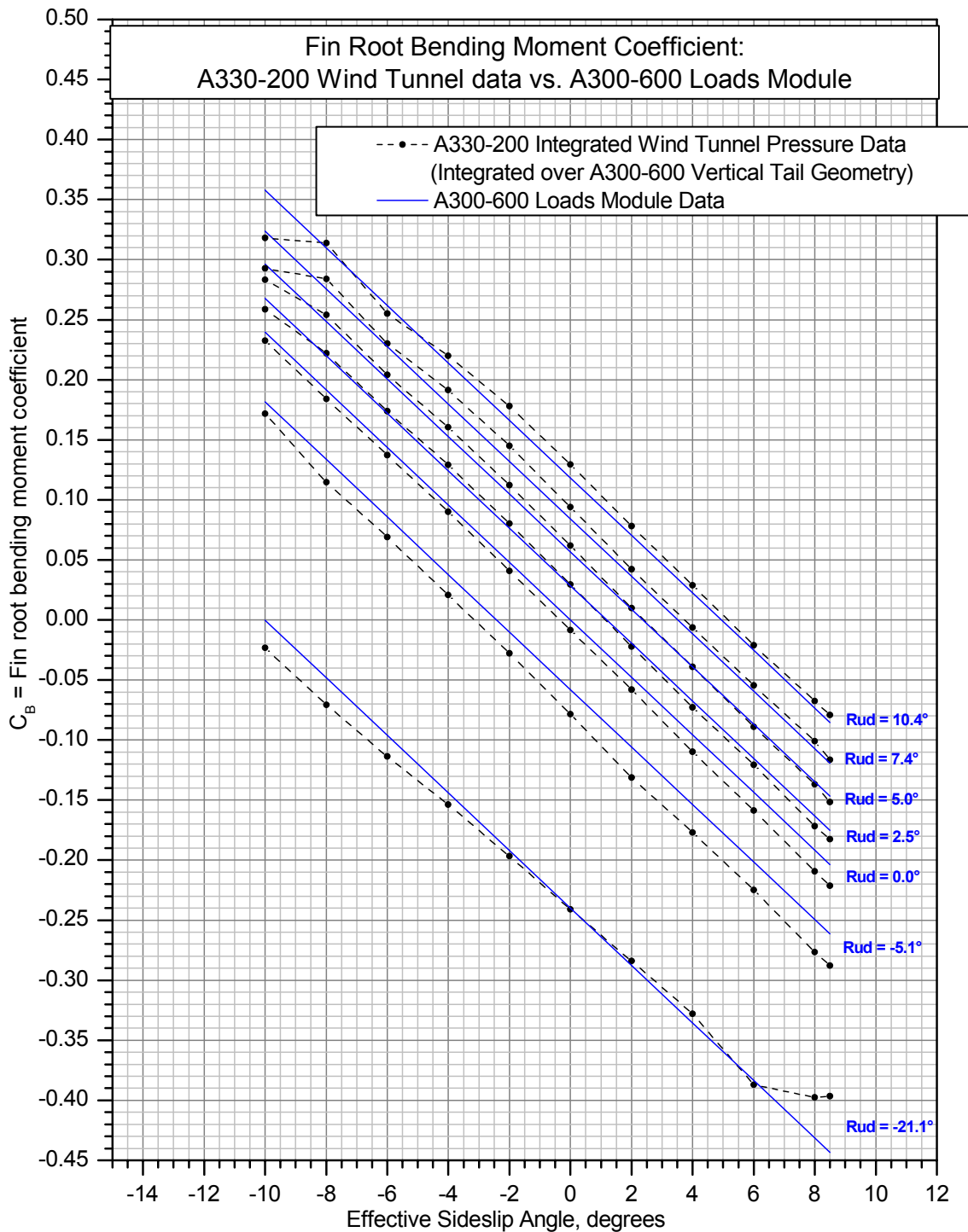


Figure 2.1.1.

CFD codes have evolved considerably over the past several years, and have yielded good prediction of flows and associated loads. However, flow separation continues to be one of the more difficult flow features to model with CFD. Several recent turbulence models have increased the accuracies of the codes, and prediction of the onset of separation (i.e., the values of angles, Reynolds numbers, and other parameters at the point flow starts to detach from the surface) is considered fairly accurate. However, the quantitative, absolute values of aerodynamic coefficients in flows with separation can still not be determined consistently with confidence. Since the wind tunnel data indicates the presence of separated flow, prior to calculation of the accident flight conditions, a calculation of the wind tunnel test results, with matching model configuration and wind tunnel conditions, was performed to test the ability of the TAU code to predict the flow features and aerodynamic coefficients indicated by the wind tunnel data. Since pressure tap data at several points on the model were available, a comparison of the wind tunnel and CFD pressure distributions can indicate if the CFD calculations are adequately capturing the onset, distribution, and extent of flow separation measured in the wind tunnel. It is assumed that any over- or under- prediction in the CFD calculation of the aerodynamic loads at the wind tunnel conditions will also be present (and can be accounted for) in the CFD calculation at the accident conditions. With the required corrections to the CFD data quantified in this way, the aerodynamic loads at the accident conditions can be estimated, including the effects of flow separation.

Table 1 lists the various load data sets (called “Configurations”) defined by the available CFD and wind tunnel data that can be used to define the load on the tail at the time of tail separation. The calculation methods described below draw on a combination of these data sets to produce a range of loads that covers the uncertainty inherent in the data sources listed in Table 1, and the differences between distinct but equally valid approaches to applying the data.

| | Accident | A330 Wind Tunnel | CFD – WT Conditions | CFD – Acc. Conditions, Rigid | CFD – Acc. Conditions, Flexible | A300 Wind Tunnel |
|----------------------|----------------|---------------------|------------------------|------------------------------------|---------------------------------------|---------------------|
| Config # | 1 | 2 | 3 | 4 | 5 | 6 |
| Airplane | A300-600 | A330-200 | A330-200 | A300-600 | A300-600 | A300B2 |
| Rigid/Flex | Flexible | Rigid | Rigid | Rigid | Flexible | Rigid |
| Scale | 1:1 | 1:34.6 | n/a | n/a | n/a | 1:28.4 |
| Re (millions) | 56.8 | 2.1 | 2.1 | 56.8 | 56.8 | 2.3 |
| M | 0.4 | 0.5 | 0.5 | 0.4 | 0.4 | 0.5 |
| α (deg.) | 1 | 2 | 2 | 1 | 1 | 0 |
| β range (deg.) | 11.3 to 14.1** | -10 to 9 | -13 to 9 | -14 to 8 | -14 to 8 | -10 to 9 |
| δ_r (deg.) | -10 to -11.5 | 7.4, 10.4, 14.8 | 10.4 | 10, 11.5 | 10, 11.5 | 10 |
| rud-fus gap | Unknown Effect | Yes | No | No | Yes | Yes |
| rud hinge gap | Unknown Effect | No | No | No | No | Yes |

The scales of the gaps for these configurations are much larger than on the real airplane in order to accommodate model balance hinges for hinge moment and tail load measurements.

** Possible β range at the moment of tail separation (see Section 3.2).

Table 1. Configuration of accident airplane and various tail load data sources.

As described in Section 3.4, the CFD computations of the load on an A330 tail at the conditions of the A330 wind tunnel test (Configuration #3 in Table 1) do not, in fact, match the wind tunnel measurements of those loads (Configuration #2), indicating that for this

problem CFD results can not be used by themselves, without correction or adjustment, to estimate absolute values of loads on a given configuration. However, the CFD results do provide a good indication of the nature and behavior of the air flow and loads (e.g., the development and growth of areas of separated flow starting near the tip, and the relative insensitivity of the bending moment to changes in β at high values of β). Furthermore, it is well established that CFD can provide very good quantitative estimates of the effects of incremental changes from one flow condition or geometry to another. An estimate of the loads on the tail at the accident conditions based on the CFD results can therefore be obtained in two ways: 1) By developing an adjustment, or transformation, that corrects the A330 wind tunnel condition CFD results to the actual wind tunnel measurements, and then applying this transformation to the A300 CFD results at accident conditions; and 2) By determining the differences between the CFD results of the A300 at accident conditions and the A330 at wind tunnel conditions, and then applying these increments to extrapolations of the A330 wind tunnel data. These two approaches are both reasonable ways of using the CFD and wind tunnel data in combination to estimate the accident condition loads, and give bending moment results that differ by about 15% at the flight condition corresponding to the tail separation. The difference in the results of the two methods represents part of the uncertainty in the loads calculation. There is an additional uncertainty in the load calculations equal to 5% of the maximum loads measured in the wind tunnel, corresponding to the experimental uncertainty inherent in the A330 wind tunnel data upon which both load calculation methods are based.

The details of the two load calculation methods are outlined below.

2.2. Computing Loads Using Wind Tunnel and CFD Data: Method 1

The first method of using the wind tunnel and CFD data in combination to estimate the loads involves developing a transformation that corrects the A330 wind tunnel condition CFD results to the actual wind tunnel measurements, and then applying this transformation to the A300 CFD results at accident conditions. It is assumed that, because the corrections themselves are relatively small, the same correction applies at both wind tunnel and accident conditions and for both the A330 and A300 geometries.

The load coefficients on the tail are primarily functions of β and δ_r , and in the linear region (the range of β where the flow is attached) can be modeled as

$$C_x = \left(\frac{\partial C_x}{\partial \beta} \right) \beta + \left(\frac{\partial C_x}{\partial \delta_r} \right) \delta_r \quad [3]$$

Where C_x is the load coefficient in question (X can represent Y for shear, B for bending, or T for torsion).

The correction to the CFD data involves determining $(\partial C_x / \partial \beta)$ and $(\partial C_x / \partial \delta_r)$ in the linear region for both the CFD results and wind tunnel data, determining the adjustment to the CFD terms that will make them match the wind tunnel terms, and then using the corrected terms to reconstruct a final, corrected CFD based C_x throughout the β range covered by

the CFD computations. $(\partial C_X / \partial \beta)$ and $(\partial C_X / \partial \delta_r)$ can be determined from the wind tunnel (WT) and CFD data as follows¹⁴:

$$\left(\frac{\partial C_X}{\partial \beta} \right)_{\text{CFD}} = \frac{[C_{X,\text{CFD}}]_{\beta=4} - [C_{X,\text{CFD}}]_{\beta=0}}{\Delta \beta} \Big|_{\delta_r = \text{const}} \quad [4a]$$

$$\left(\frac{\partial C_X}{\partial \beta} \right)_{\text{WT}} = \frac{[C_{X,\text{WT}}]_{\beta=4} - [C_{X,\text{WT}}]_{\beta=0}}{\Delta \beta} \Big|_{\delta_r = \text{const}} \quad [4b]$$

$$\left(\frac{\partial C_X}{\partial \delta_r} \right)_{\text{CFD}} = \frac{[C_{X,\text{CFD}}]_{\beta=0}}{\Delta \delta_r} \quad [5a]$$

$$\left(\frac{\partial C_X}{\partial \delta_r} \right)_{\text{WT}} = \frac{[C_{X,\text{WT}}]_{\beta=0}}{\Delta \delta_r} \quad [5b]$$

The ratios of the wind tunnel to CFD terms represent the correction factors to the CFD terms:

$$k_\beta = \frac{(\partial C_X / \partial \beta)_{\text{WT}}}{(\partial C_X / \partial \beta)_{\text{CFD}}} \quad [6a]$$

$$k_{\delta_r} = \frac{(\partial C_X / \partial \delta_r)_{\text{WT}}}{(\partial C_X / \partial \delta_r)_{\text{CFD}}} \quad [6b]$$

The corrected CFD results are then obtained as

$$(C_{X,\text{CFD}})_{\text{CORRECTED}} = (C_{X,\text{CFD}} - C_{X,\text{CFD}}|_{\beta=0})k_\beta + (C_{X,\text{CFD}}|_{\beta=0})k_{\delta_r} \quad [7]$$

The k_β and k_{δ_r} factors for shear, bending and torsion are shown in Table 2.

| | k_β | k_{δ_r} |
|-------------------|-----------|----------------|
| Shear (C_Y) | 0.94 | 0.85 |
| Bending (C_B) | 0.94 | 0.85 |
| Torsion (C_T) | 0.94 | 0.84 |

Table 2. Values of k_β and k_{δ_r} used to correct CFD data.

¹⁴ Before Equations [4b] and [5b] are evaluated, the wind tunnel data is shifted to enforce symmetry (i.e., loads = 0 at $\beta = 0$ and $\delta_r = 0$). The increments in C_Y , C_B , and C_T required to achieve this symmetry are applied to all combinations of β and δ_r .

2.3. Computing Loads Using Wind Tunnel and CFD Data: Method 2

The second method of using the wind tunnel and CFD data in combination to estimate the loads involves determining the differences between the CFD results of the A300 at accident conditions and the A330 at wind tunnel conditions, and then applying these increments to extrapolations of the A330 wind tunnel data. It is assumed that the CFD increments capture the effects of changing flight condition and airplane geometry, and that these increments, when added to the A330 wind tunnel data, represent the A300 at accident conditions.

This method is more complicated than Method 1 because there are several adjustments that have to be made to the CFD data before the wind tunnel to flight increments can be computed, and because the wind tunnel data to which the increments are added needs to be extrapolated to the higher β range of interest (though the behavior of the CFD loads can help guide this extrapolation, as discussed below). Furthermore, accounting for the effects of flexibility is less straightforward, as the wind tunnel data is rigid (in contrast, the transformations determined with Method 1 can be applied directly to the flexible CFD solution). Flexibility effects are accounted for in this method by using a comparison of the rigid and flexible CFD results to determine an effective reduction in the sideslip angle due to elastic deformation of the aft body and vertical tail, and then assuming that the flexible load at the actual β is equal to the rigid load at the reduced β .

The loads at $\delta_r = 10^\circ$ are calculated by obtaining the $\delta_r = 11.5^\circ$ to $\delta_r = 10^\circ$ load increments from the Configuration 2 data in Table 1, and then applying these increments to the Method 2 $\delta_r = 11.5^\circ$ solution. The loads at $\delta_r = 10^\circ$ account for the uncertainty in the rudder angle at the time of tail separation, as described in Section 3.3. At a given δ_r , Method 2 gives consistently lower loads than Method 1, and lower rudder angles also produce lower loads. Hence, using Method 2 to calculate loads at $\delta_r = 10^\circ$ and Method 1 to compute the loads at $\delta_r = 11^\circ$ results in the largest possible range in tail loads associated with the uncertainties in the aerodynamic coefficients and rudder angle.

The steps outlined above are described in more detail in what follows.

2.3.1. Calculating A330 Wind Tunnel Conditions to A300 Accident Conditions Increments

Examining Table 1, it would appear that the A330 wind tunnel conditions to A300 accident conditions increments correspond to the difference between Configurations 4 and 3, after the data for these configurations has been corrected using Equation [7]. However, Configuration 4 corresponds to a δ_r of 11.5° , and Configuration 3 corresponds to a δ_r of 10.4° . Consequently, Configuration 3 has to be adjusted to $\delta_r = 11.5^\circ$ before it can be subtracted from Configuration 4. These adjustments can be determined from the $\delta_r = 10.4^\circ$ and 14.8° runs from Configuration 2¹⁵, by first interpolating between these runs to obtain a solution for $\delta_r = 11.5^\circ$, and then subtracting the results for $\delta_r = 10.4^\circ$ from the solution for $\delta_r = 11.5^\circ$. Mathematically, the operations can be represented as

$$\Delta C_x \Big|_{\delta_r=11.5}^{C4'-C3'} = C_x \Big|_{\delta_r=11.5}^{C4'} - \left\{ C_x \Big|_{\delta_r=10.4}^{C3'} + \left(C_x \Big|_{\delta_r=11.5}^{C2} - C_x \Big|_{\delta_r=10.4}^{C2} \right) \right\} \quad [8]$$

where

¹⁵ Before data from Configuration #2 is used, it is adjusted to enforce symmetry (the need for this adjustment can be seen in the non-zero value of C_B at $\beta = 0$ and $\delta_r = 0$ in the wind tunnel data plotted in Figure 2.1.1).

$C_{X|_{\delta_r=11.5}}^{C2}$ are the C_X for Configuration 2 at $\delta_r = 11.5^\circ$, obtained by linear interpolation between the C_X for Configuration 2 at $\delta_r = 10.4^\circ$ and 14.8° .

In this nomenclature, C2, C3, and C4 refer to Configurations in Table 1, and a prime (') indicates that the data has been corrected using Equation [7]. The ΔC_X in Equation [8] represent the A330 wind tunnel conditions to A300 accident conditions load coefficient increments, for $\delta_r = 11.5^\circ$.

2.3.2. Extrapolating the A330 Wind Tunnel Data to Higher Sideslip Angles

Since the increments developed in Equation [7] are to be applied to the A330 wind tunnel data (Configuration 2 in Table 1), this data must be extrapolated to the same β at which the CFD data (Configurations 3 and 4) are defined, i.e., out to -13° ¹⁶. The difficulty of extrapolating this data is one of the reasons the CFD study was initiated, and the CFD results can be used to guide the extrapolation.

The data for Configurations 3, 4 and 5, presented in Section 3 of this *Addendum*, indicate that for the (flexible) tail up to $\beta = -13^\circ$, the loads behave as follows:

Shear: The shear load is continuing to increase at $\beta = -10^\circ$, and can be extrapolated to $\beta = -13^\circ$ assuming the same slope that exists between $\beta = -8^\circ$ and $\beta = -10^\circ$ with little error. C_Y for Configuration 2 is extrapolated to $\beta = -13^\circ$ in this manner.

Bending: Once the slope of the C_B vs. β curve flattens out, it tends to remain flat and does not drop precipitously. Based on this observation and the very small slope in the C_B vs. β curve between $\beta = -8^\circ$ and -10° in the Configuration 2 data, C_B for this data is extrapolated to $\beta = -13^\circ$ by holding the C_B value measured at $\beta = -10^\circ$.

Torsion: Once the slope of the C_T vs. β curve flattens out, it tends to remain nearly flat, and does not drop precipitously (though at $\delta_r = 11.5$, C_T drops a bit between $\beta = -13^\circ$ and -14°). Based on this observation and the very small slope in the C_T vs. β curve between $\beta = -8^\circ$ and -10° in the Configuration 2 data, C_T for this data at $\delta_r = 10^\circ$ and 11° is extrapolated to $\beta = -13^\circ$ by holding the C_T value measured at $\beta = -10^\circ$.

These extrapolation methods are further supported by additional A330-200 wind tunnel data showing the contribution of the vertical and horizontal stabilizers to the total airplane side force coefficient, out to $\beta = 30^\circ$. These data are obtained from balance measurements (not pressure measurements) and so indicate the total side force contribution of the tails, but do not allow the shear, bending, and torsion forces on the tails themselves to be computed. Nonetheless, the data show that the side force due to the tails is linear with β up to about $\beta = 10^\circ$ (consistent with the CFD data), and then starts to become non-linear, flattening out and remaining constant with increasing β out to $\beta = 30^\circ$. This behavior is observed for all rudder deflections, from -35° to 35° , and indicates that the contribution of the tails to the aerodynamic forces on the airplane does not decrease with increasing β in

¹⁶ Configuration 3 data runs to $\beta = -13^\circ$, and Configuration 4 data runs to $\beta = -14^\circ$; hence, the difference between the two is only available up to $\beta = -13^\circ$. Consequently, Configuration 2 data is extrapolated to 13° . Final Method 2 loads at $\beta = 14^\circ$ are obtained by extrapolating from the final results at $\beta = 13^\circ$.

the non-linear region. Consistent with these observations for the side force, the torsion and bending moments for the Method 2 extrapolations are held constant beyond $\beta = 10^\circ$.

The behavior seen in the Airbus data for side force at higher sideslip angles was compared with data available for other configurations of vertical tails. Wind tunnel data and CFD data from other manufacturers was examined, along with wind tunnel experimental data for several generic tails with varying sweep and aspect ratios.¹⁷ All data examined showed a similar behavior of side force after the onset of nonlinearity, with little, if any, reduction in side force with increasing sideslip angle for all configurations examined. This comparison provided confidence that the Airbus data reflected a proper treatment of the higher sideslip behavior for the Airbus A300-600.

A final adjustment to the extrapolated Configuration 2 data is made to make the data match the A300-600 LLM in the linear range of β . This is done because the LLM is based on the original A300 wind tunnel data¹⁸, and represents the best estimate at the time the airplane was designed of the loads on the tail at wind tunnel conditions.

2.3.3. Accounting for Flexibility Effects

Adding the increments described by Equation [8] to the extrapolated Configuration 2 data just discussed yields the final Method 2 estimates of the rigid loads for the A300-600 at accident conditions. However, the actual accident loads include the effects of flexibility, and so these effects must be considered.

Configuration 5 in Table 1 represents a very sophisticated CFD and finite element method (FEM) computation of the loads on the tail, including the deformation of the tail structure under load. Comparing the results of Configurations 4 and 5 (see Section 3.4) indicates that in the linear region, flexibility effects tend to reduce the load at a given β , and that in the non-linear region, the flexibility effects decrease, until at some sufficiently high β , the flexible solution and rigid solution converge. A simple model of this behavior consists of the vertical tail mounted on a torsional spring, which deflects in proportion to the load on the tail. The deflection results in an effective reduction in the β seen by the tail, which (if β isn't too large) decreases the load. The resulting load on the tail is that which balances the spring force, which will generally be lower than the rigid load at the same β . Equivalently, the flexible load at a given β is equal to the rigid load at a reduced β , where the β reduction is itself a function of the load. Note that if β is sufficiently high, in the region where the C_B vs. β curve is flat, a reduction in β may not result in a reduction in load. This is consistent with the convergence of the rigid and flexible C_B and C_T loads seen in the data for Configurations 4 and 5.

To incorporate flexibility effects into the Method 2 estimates of tail loads, the data from Configurations 4 and 5 (corrected using Equation [7]) is used to produce a table of β decrements ($\Delta\beta$) vs. rigid loads. The $\Delta\beta$ are those required to make the rigid (Configuration 4) loads equal to the flexible (Configuration 5) loads at the same (original) β . To then determine the flexible loads based on the Method 2 rigid loads, the rigid load is used to

¹⁷ See references 9, 10, and 11.

¹⁸ The original A300B2 wind tunnel data (including Configuration #6 in Table 1) required significant corrections before being used as the basis for the LLM. These corrections are discussed further in Section 2.6 of this *Addendum*.

determine the $\Delta\beta$ from the table, the $\Delta\beta$ is applied to the original β , and the rigid load corresponding to the reduced β is retrieved as the flexible load at the original β .

Mathematically, these operations can be described as follows. Before the flexible loads can be calculated, the $\Delta\beta$ table must be constructed from Configurations 4 and 5:

$\Delta\beta = f(C_{X,RIGID})$ from Configurations 4 & 5, such that

$$C_X|_{\beta}^{C5'} = C_X|_{\beta-\Delta\beta}^{C4'} \quad [9]$$

A different $\Delta\beta$ table is required for shear, bending, and torsion. These $\Delta\beta$ tables are then used to calculate the final, flexible Method 2 loads at accident conditions from the final, rigid Method 2 loads. First, the applicable $\Delta\beta$ is found from the rigid load and $\Delta\beta$ table:

$\Delta\beta = f(C_X|_{\beta}^{M2,RIGID})$ from $\Delta\beta$ table. Here, "M2, RIGID" refers to the rigid Method 2 loads.

Then, the $\Delta\beta$ is used along with the Method 2 rigid load data to evaluate the flexible load:

$$C_X|_{\beta}^{M2,FLEX} = C_X|_{\beta-\Delta\beta}^{M2,RIGID} \quad [10]$$

The "M2, FLEX" are the final, flexible Method 2 loads for $\delta_r = 11.5^\circ$.

2.3.4. Computing Method 2 Loads at Rudder = 10°

The Method 2 calculations outlined in the previous sections result in load estimates for $\delta_r = 11.5^\circ$. As described in Section 3.3, exact value of δ_r at the moment of tail separation is uncertain, but probably lies in the range from $\delta_r = 10^\circ$ to $\delta_r = 11^\circ$. An estimate of the loads at $\delta_r = 10^\circ$ can be obtained by calculating the load increments from $\delta_r = 11.5^\circ$ to $\delta_r = 10^\circ$ from the configuration 2 data, and then applying these increments to the Method 2 solution at $\delta_r = 11.5^\circ$. Mathematically, these calculations can be expressed as

$$C_X|_{\delta_r=10.0}^{M2,FLEX} = C_X|_{\delta_r=11.5}^{M2,FLEX} + \left\{ C_X|_{\delta_r=10.0}^{C2} - C_X|_{\delta_r=11.5}^{C2} \right\} \quad [11]$$

where $C_X|_{\delta_r=10.0}^{M2,FLEX}$ are the Method 2, flexible loads at $\delta_r = 10^\circ$, $C_X|_{\delta_r=11.5}^{M2,FLEX}$ are the Method 2, flexible loads at $\delta_r = 11.5^\circ$, and $C_X|_{\delta_r=10.0}^{C2}$ and $C_X|_{\delta_r=11.5}^{C2}$ are the Configuration 2 loads from Table 1 at $\delta_r = 10^\circ$ and 11.5° , respectively¹⁹. The Configuration 2 loads at $\delta_r = 10^\circ$ and 11.5° are obtained from linear interpolation of the Configuration 2 data for $\delta_r = 7.4^\circ$, 10.4° , and 14.8° . The Configuration 2 load increments from $\delta_r = 11.5^\circ$ to 10.4° corresponding to sideslip angles greater than 10° (beyond the range of the Configuration 2 data) are assumed to be equal to the increments at $\beta = 10^\circ$. This is a conservative assumption, as the increments decrease slowly with increasing β .

¹⁹ A similar method is used to obtain the Method 2 loads at $\delta_r = 11^\circ$ presented in Section 3.5.

2.4. “Effective” Sideslip Angle Resulting From Dynamic Effects

The β at the CG of the airplane (β_{CG}) is not, in general, equal to the β at the vertical tail, because of the sidewash angle (the deflection of the airflow by the wing and fuselage) and dynamic effects. The dynamic effects include β increments induced by yaw rate, and β rate effects, which arise from the time required for β changes at the CG to affect the sidewash at the tail.

The Linear Loads Module accounts for all of these effects and determines the load on the tail based on β at the vertical tail. The CFD and wind tunnel Configurations listed in Table 1, however, describe the load data as a function of β_{CG} , with all dynamic effects equal to zero. Using the CFD and wind tunnel data to determine the load on the tail at the dynamic conditions of the accident therefore requires adjusting β_{CG} to account for the β increments resulting from yaw rate and β rate:

$$\beta_{EFF} = \beta_{CG} + \Delta\beta_R + \Delta\beta_{\dot{\beta}} \quad [12]$$

Where $\Delta\beta_R$ is the β increment due to yaw rate, $\Delta\beta_{\dot{\beta}}$ is the β increment due to β rate, and β_{EFF} is the resulting “effective” sideslip angle. No increment is needed for sidewash, because sidewash is inherent in the wind tunnel and CFD data. $\Delta\beta_R$ and $\Delta\beta_{\dot{\beta}}$ are determined using the equations defined in the LLM, which use the airplane state as input. The loads based on wind tunnel and CFD data are then determined as a function of β_{EFF} rather than β_{CG} .

A comparison of β_{CG} and β_{EFF} is shown in Figure 2.4.1 for the minimum and maximum values of heading latency (170 ms and 320 ms, respectively).

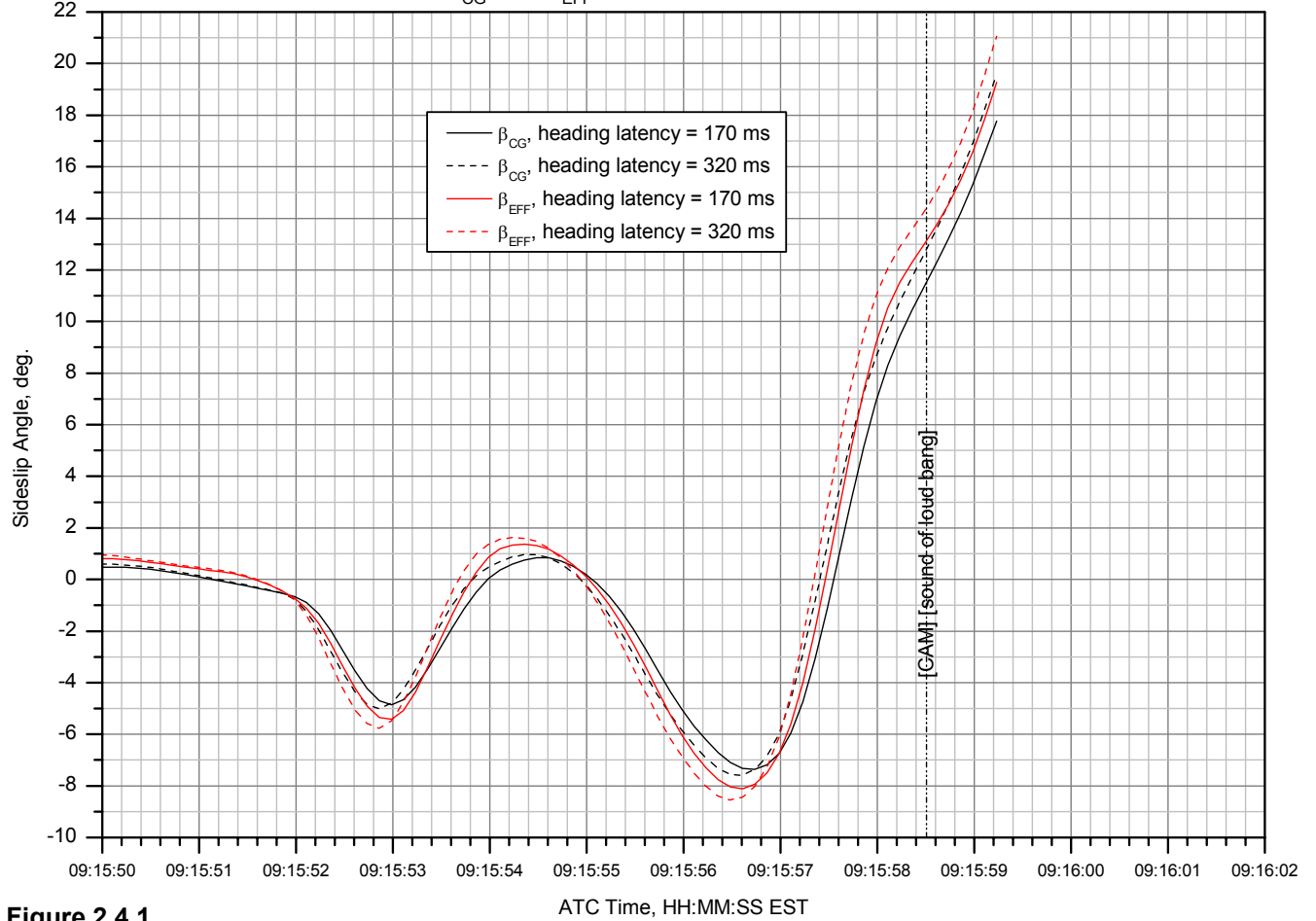
Comparison of β_{CG} and β_{EFF} at Minimum and Maximum Heading Latency

Figure 2.4.1.

2.5. Coordinate Systems

As mentioned in Section 1.6, the vertical tail loads are expressed in both airplane coordinates and vertical tail structural coordinates. These coordinate systems are shown in Figure 2.5.1. The y axes for both systems are into the page. The loads can be transformed from one system to another using the following relationships:

$$\begin{Bmatrix} C_B \\ C_Y \\ C_T \end{Bmatrix}_V = [T_{AV}] \begin{Bmatrix} C_B \\ C_Y \\ C_T \end{Bmatrix}_A \quad [13]$$

where the subscripts V and A indicate components in vertical tail and airplane coordinates, respectively, and the transformation matrix $[T_{AV}]$ is given by

$$[T_{AV}] = \begin{bmatrix} -\cos \theta & 0 & \sin \theta \\ 0 & 1 & 0 \\ -\sin \theta & 0 & -\cos \theta \end{bmatrix} \quad \text{with } \theta = 37.74^\circ \quad [14]$$

Since $[T_{AV}]$ is orthogonal,

$$\begin{Bmatrix} C_B \\ C_Y \\ C_T \end{Bmatrix}_A = [T_{AV}]^{-1} \begin{Bmatrix} C_B \\ C_Y \\ C_T \end{Bmatrix}_V = [T_{AV}]^T \begin{Bmatrix} C_B \\ C_Y \\ C_T \end{Bmatrix}_V \quad [15]$$

Note that the bending moment is the moment about the positive x axis for each system, the torsion moment is the moment about the positive z axis for each system, and the shear force is parallel to the positive y axis, which is identical for the two systems.

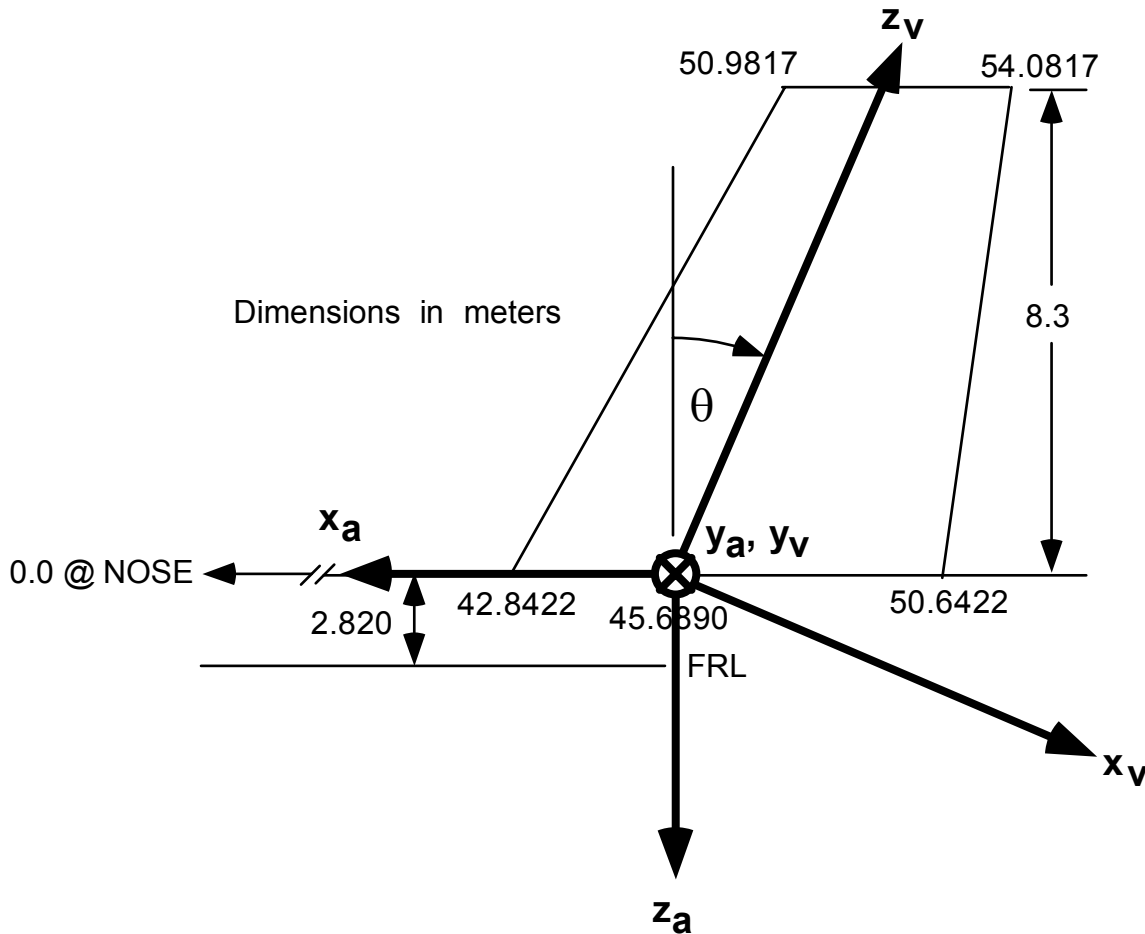


Figure 2.5.1. Airplane (x_a, y_a, z_a) and vertical tail structural (x_v, y_v, z_v) coordinate systems. $\theta = 37.74^\circ$.

2.6. A300B2 Wind Tunnel Data

As mentioned above, the A300B2 wind tunnel data (Configuration 6 in Table 1) is the basis of the Linear Loads Module used by Airbus to determine vertical tail loads during the design of the airplane. Note, however, that Configuration 6 data is not used in either Method 1 or Method 2 (described above) to calculate loads on the tail. Even though Configuration 6 is the basis of the LLM, the Configuration 6 data contains several inaccuracies that must be corrected before the data can be used. After the corrections are applied, the result closely matches the LLM in the linear region. Hence the corrected Configuration 6 data is consistent with the basis of the loads estimates described by Methods 1 and 2.

Some of the differences between the Configuration 6 data and the full-scale airplane characteristics result from gaps on the wind tunnel model along the rudder hinge line between the vertical tail and the rudder, and between the vertical tail root and the fuselage. The gaps are required for clearance so that loads on the rudder and vertical tail can be measured with strain-gage balances²⁰. Air can flow through these gaps, changing the aerodynamic forces acting on the tail; in particular, the rudder hinge line gap can allow air from the high pressure surface to leak towards the low pressure surface, energizing the boundary layer and delaying flow separation. This behavior is not representative of the actual aircraft, and renders the A300B2 wind tunnel data inadequate for studying the loads behavior at the high β values of interest, where flow separation effects are important.

Another source of inaccuracy in the data is the use of strain-gage balances on the rear fuselage, vertical tail, and rudder, which introduce flexibility into the model and decrease the load measurements.

As a result of the flexibility and gap effects, the Configuration 6 data shows significantly lower loads than the LLM and the A330 wind tunnel data (Configuration 2), and shows little evidence of non-linearity (flow separation) at higher β angles.

Table 3 lists the corrections to the Configuration 6 data that Airbus indicates are required to account for the effects described above. These corrections are based on Airbus' experience, guided by wind tunnel to flight test comparisons over several airplane models, in testing wind tunnel models outfitted with strain-gage balances in the aft body and on the control surfaces. Note that these corrections are in the form of a "sideslip effect" and "rudder effect;" these terms are essentially the same as the correction factors k_β and k_{δ_r} described in Section 2.2. Using $k_\beta = 1.065$ and $k_{\delta_r} = 1.165$ in Equation [7] to correct the A300B2 wind tunnel data at $\delta_r = 10^\circ$ gives the result presented in Figure 2.6.1, which shows the good agreement between the corrected data and the LLM.

| | Sideslip Effect | Rudder Effect |
|---------------------------------------|-----------------|---------------|
| Rear end flexibility | 0.7% | 0.8% |
| Root balance flexibility | 1.1% | 2.3% |
| Rudder flexibility | 0.3% | 1.5% |
| Fin root gap | 2.0% | 2.0% |
| Rudder gap / unknown | 0.4% | 7.9% |
| Root balance vs. pressure integration | 2.0% | 2.0% |
| Total | 6.5% | 16.5% |

Table 3. Summary of correction factors to A300B2 wind tunnel data, as provided by Airbus.

²⁰ The data recovered from the Configuration 6 test in September 2003 only included pressure data over the vertical tail and rudder; the loads data measured with the strain-gage balances was not recovered.

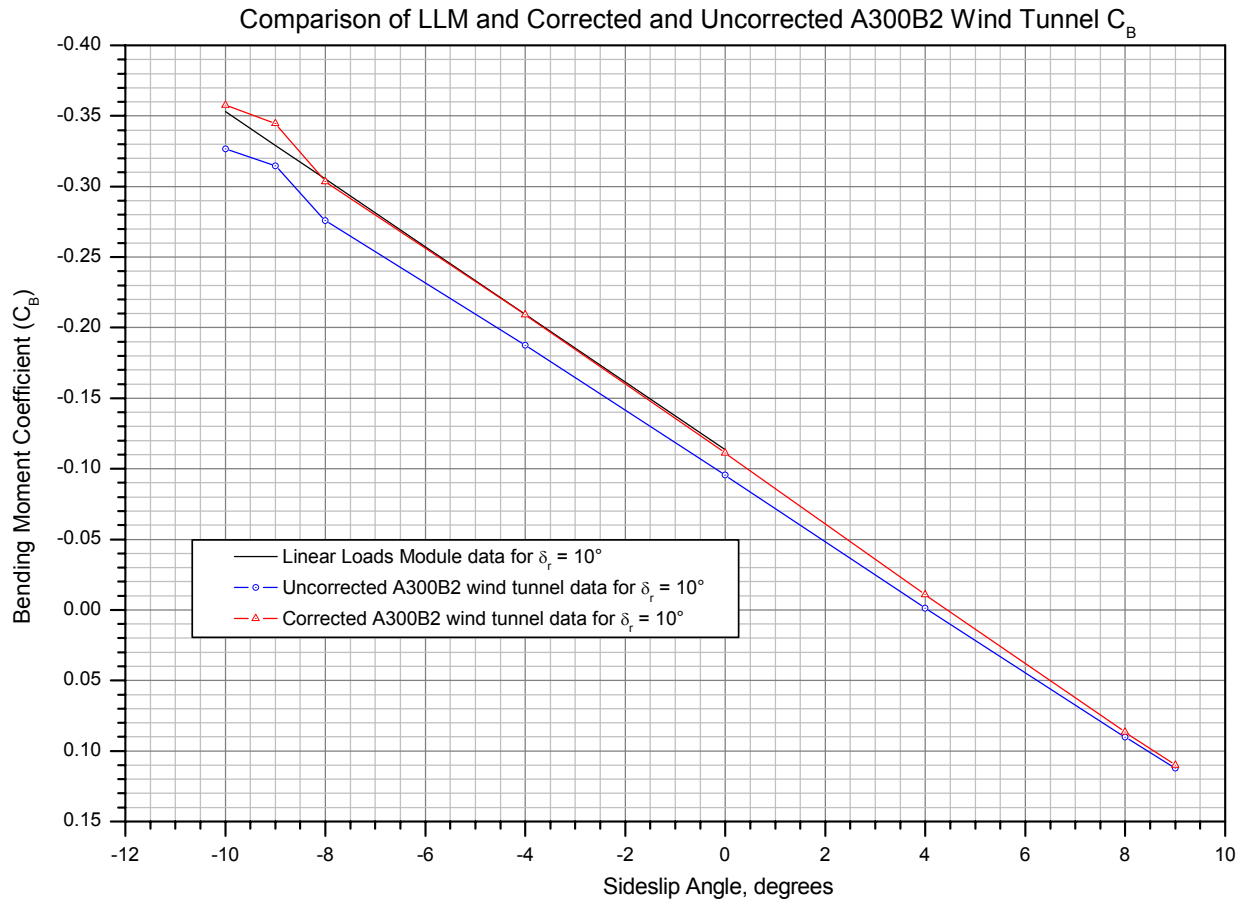
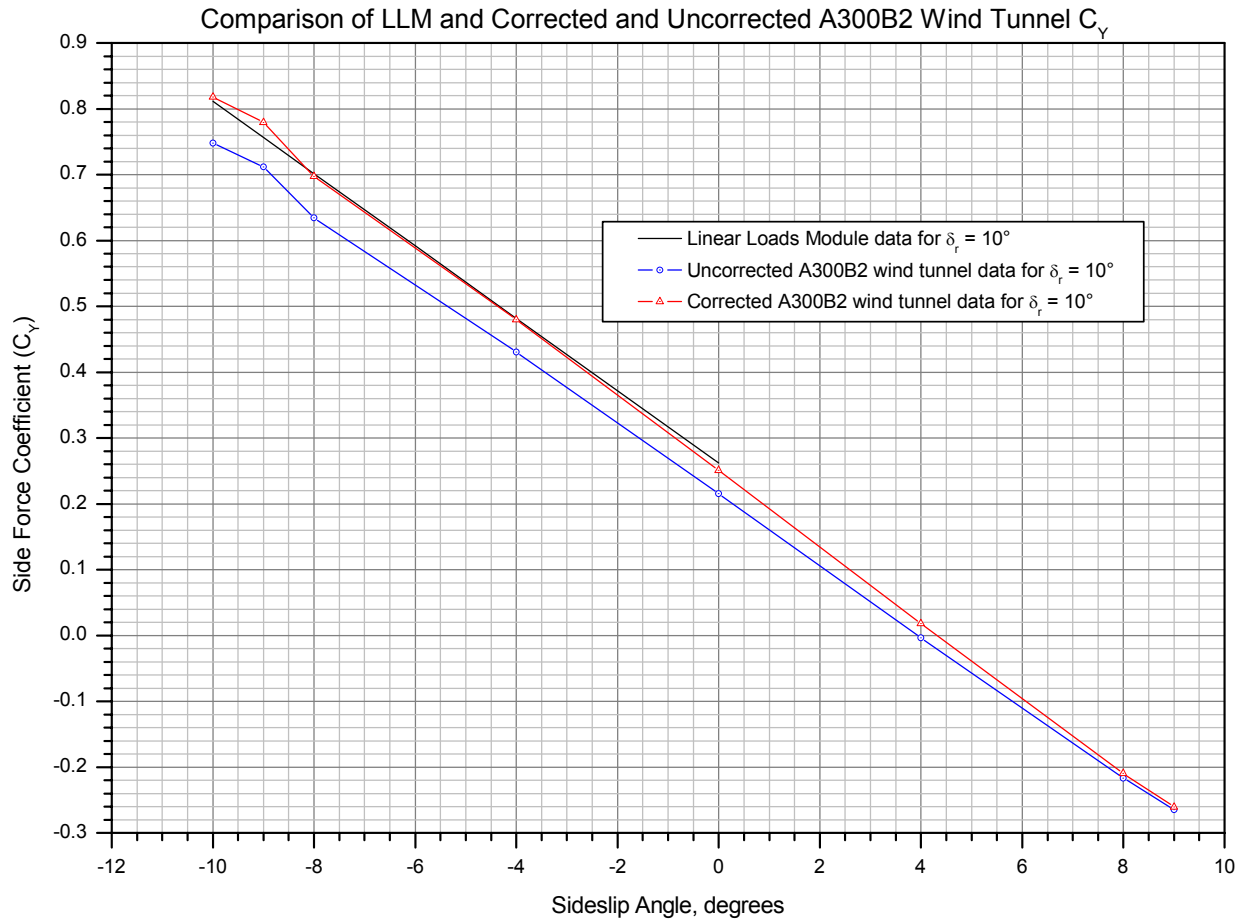


Figure 2.6.1.

3. RESULTS

3.1. Uncertainty in Sideslip Angle

3.1.1. Uncertainty Due to Data Latency

Section 2.1 of *Addendum 1* lists the potential delays in the Euler angles as follows:

| <u>Parameter</u> | <u>Latency (ms)</u> |
|------------------|---------------------|
| Pitch angle | 80 to 150 |
| Roll angle | 80 to 150 |
| Magnetic Heading | 170 to 320 |

To determine the range in β resulting from different combinations of these latencies, β was calculated using the method described in Section D-IV of the *Aircraft Performance Study* for the following cases:

| Case # | Pitch Latency (sec.) | Roll Latency (sec.) | Heading Latency (sec.) |
|--------|----------------------|---------------------|------------------------|
| 1 | 0.080 | 0.080 | 0.170 |
| 2 | 0.080 | 0.080 | 0.320 |
| 3 | 0.150 | 0.150 | 0.170 |
| 4 | 0.150 | 0.150 | 0.320 |

Figure 3.1.1 shows the β calculations corresponding to these four different combinations of pitch, roll, and heading angle latencies. Note that at a given value of heading latency, changes in the pitch and roll latencies have negligible effect on the β calculation.

3.1.2. Uncertainty Due to Sideslip Angle Calculation Method

Section D-IV of the *Aircraft Performance Study* describes how β is computed based on the integration of the FDR load factor data (this is the β used for computing the loads on the tail). The calculation involves computing the acceleration along each airplane axis, which in turn requires the time history of the angular rates (pitch, roll, and yaw) about those axes, which are obtained by taking time derivatives of interpolations through the recorded pitch, roll, and heading angles. In addition, the velocity of the airplane relative to the air (which determines β) is computed from the vector relationships between airspeed, wind speed, and groundspeed, requiring assumptions about the wind speed and direction during the period where β is of interest.

The finite sample rate of the FDR pitch, roll and heading parameters allow for some diversity in possible interpolations between the recorded points, which will result in slightly different angular rates and sideslip angle results. Different methods for accounting for winds during the integration of the load factor data can also result in differences in the resulting β . These variables introduce uncertainty into the β calculation.

Effect of Data Latency on Sideslip Angle Calculation

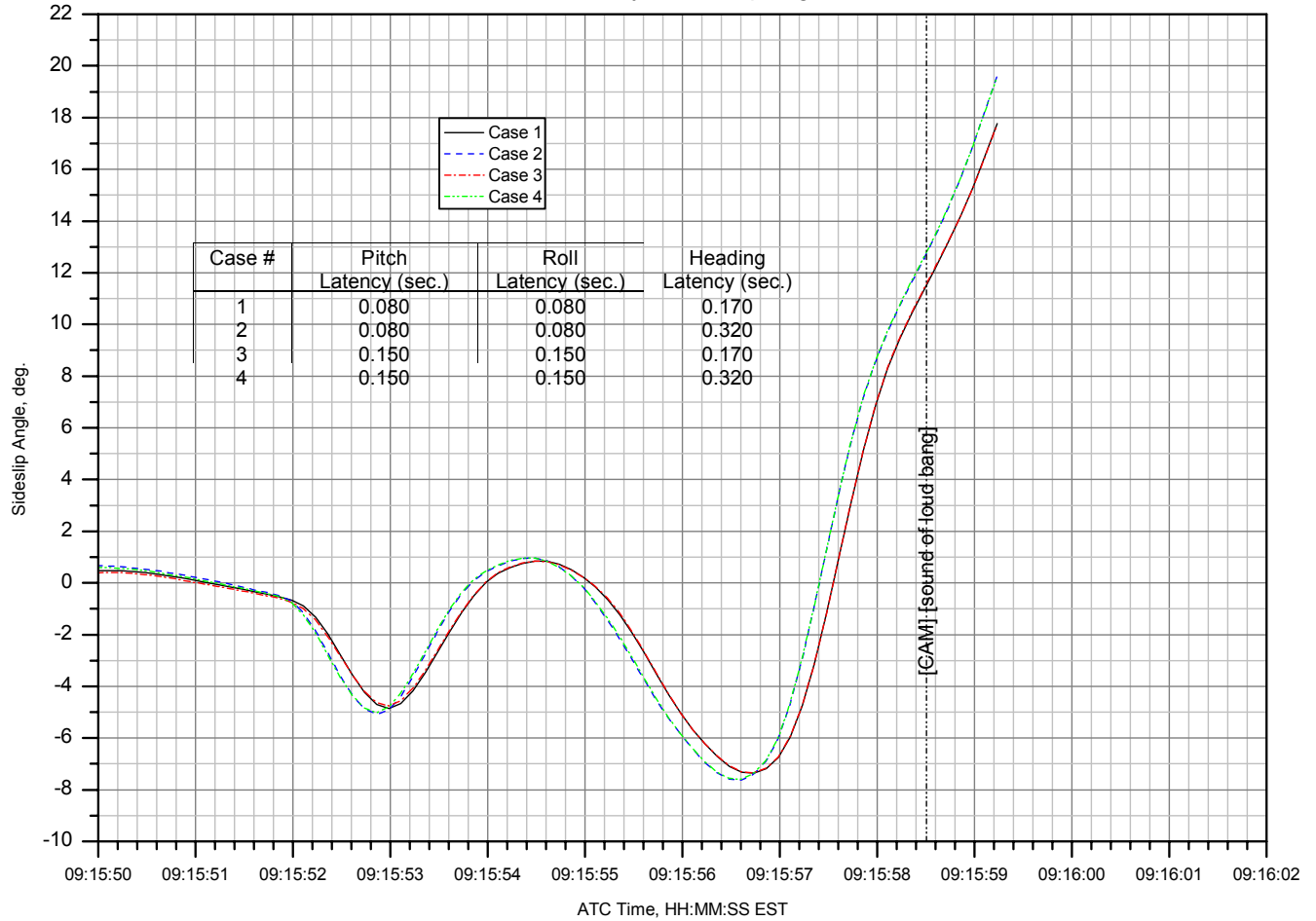


Figure 3.1.1.

Figure 3.1.2 shows two different interpolations through the recorded heading data²¹, Figure 3.1.3 shows two different wind estimates, and Figure 3.1.4 shows the two different β calculations resulting from the different heading interpolations and wind estimates. The “NTSB β Calculation” uses the “NTSB heading interpolation” and “NTSB winds.” The “Airbus β Calculation” uses the “Airbus heading interpolation” and “Airbus winds.”²² Figures 3.1.2 and 3.1.4 show that the different interpolation methods can result in heading angle differences of up to a degree in places, and that these differences (along with the effect of the different wind estimates) are reflected in the β calculations. After 09:15:56.5 and approaching the “sound of loud bang” recorded on the CVR (at 09:15:58.5), the NTSB β calculation is consistently about 1 degree more positive than the Airbus calculation. Passing through 09:15:58.2, the NTSB calculation becomes slightly lower than the Airbus calculation. Based on these results, an overall β uncertainty of $+0.5^\circ / -1^\circ$ in the NTSB β around the “sound of loud bang” is attributed to the β calculation method.

²¹ For both heading interpolations, a latency of 0.250 seconds on the original recorded data is assumed.

²² The Airbus β calculation method is described in Reference 6.

Airbus and NTSB Interpolations Through Heading Data Points

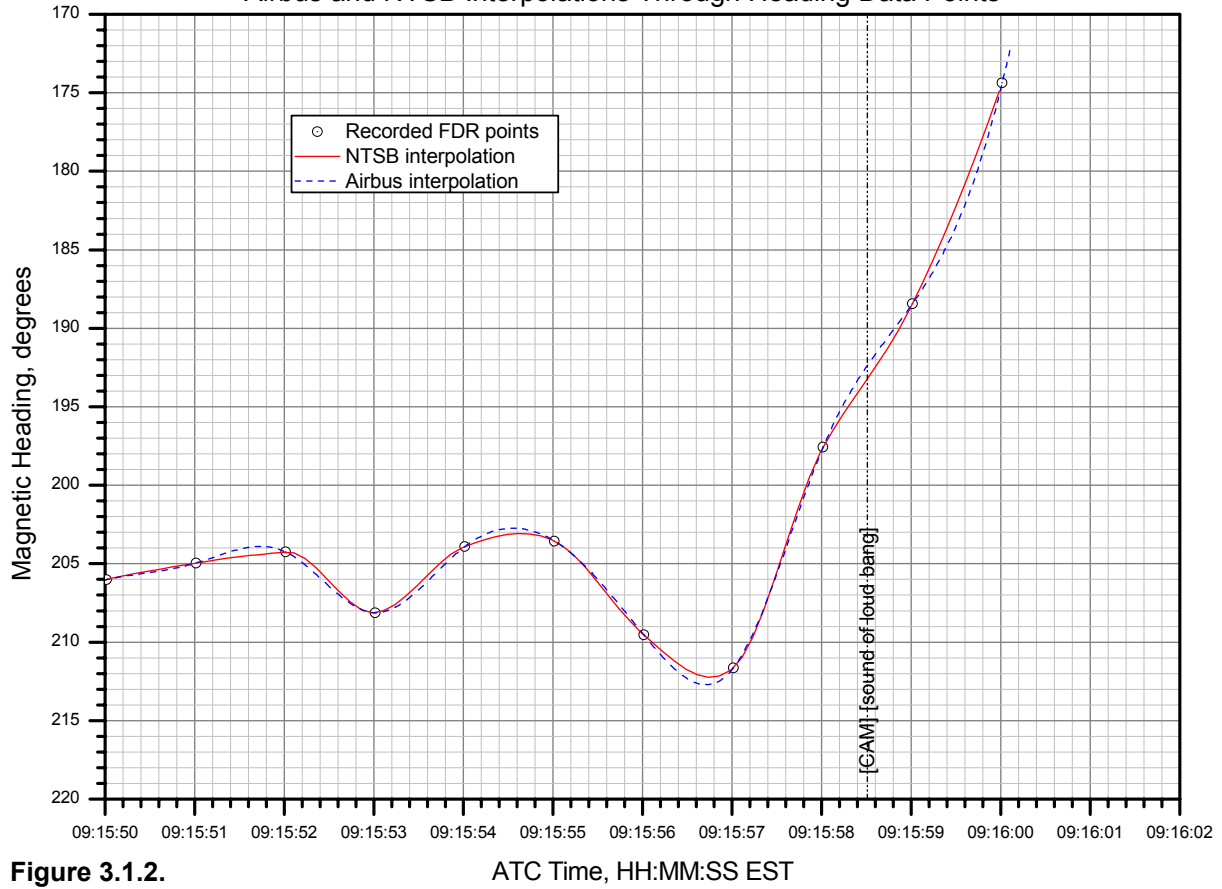


Figure 3.1.2. ATC Time, HH:MM:SS EST

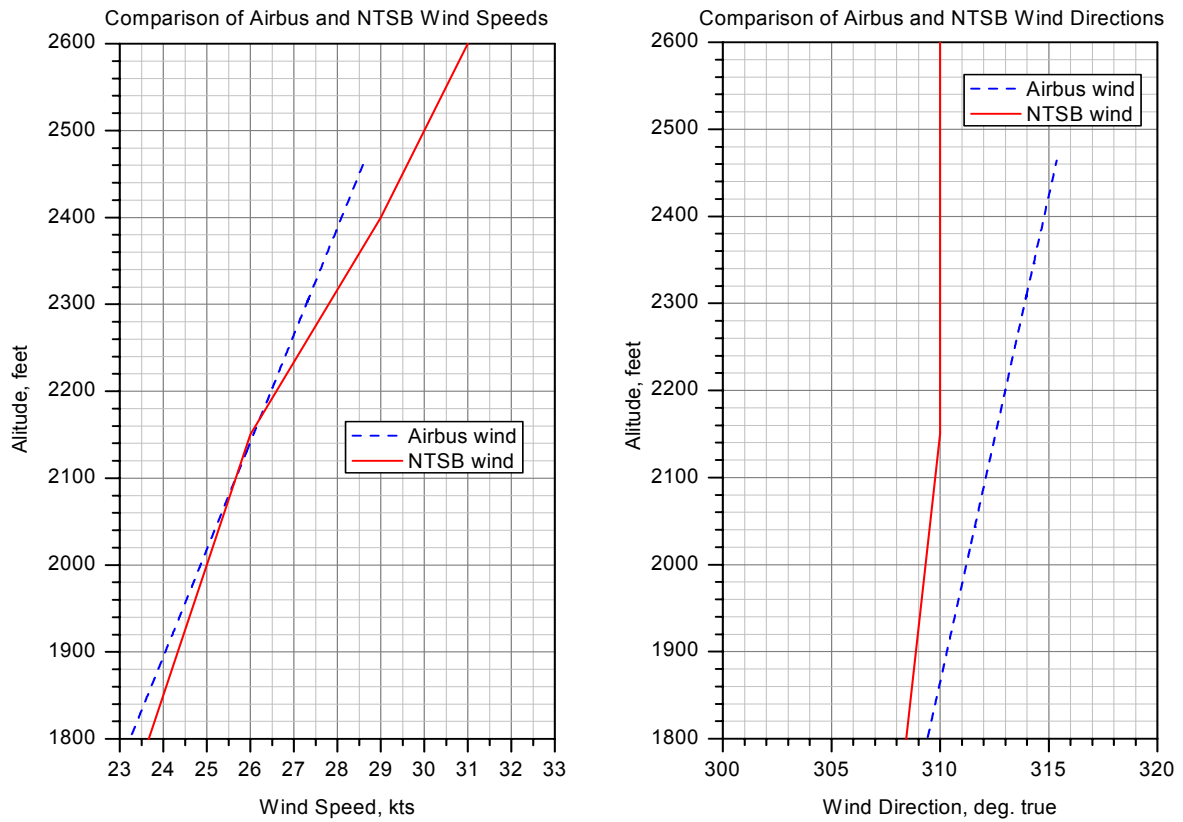
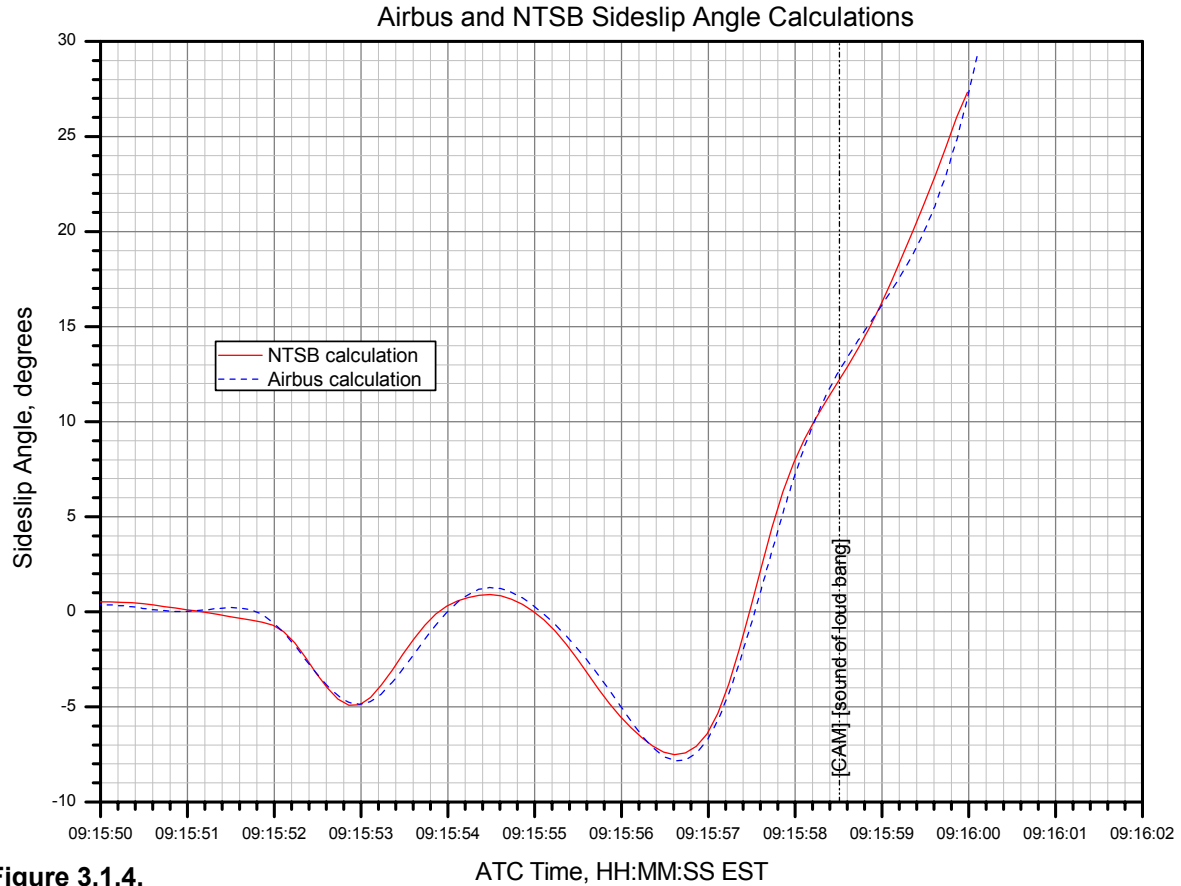


Figure 3.1.3.



3.2. Sideslip Angle Range at Time of Vertical Tail Separation

To determine the value of β at the time of tail separation, the time of tail separation must first be identified. In the *Aircraft Performance Study*, this moment was identified as coincident with the “sound of loud bang” recorded on the CVR; tail separation at this time is consistent with the 0.2 g lateral load factor jump recorded on the FDR, and the simulator matches of the accident presented in the *Study* and in *Addendum 1*. Assuming, then, that the loud bang is indeed produced by the fracturing of the vertical tail attachment lugs, a more precise estimate of the time of fracture can be obtained by accounting for the time it takes sound to travel from the rear of the airplane to the CVR area microphone through the air in the fuselage²³.

The distance from the tail to the cockpit is about 157 feet, and so it would take a sound 0.14 seconds to travel that distance in air at 68° F. The lug fracture would therefore have occurred 0.14 seconds before the sound of the fracture was recorded, or at 09:15:58.51 – 0.14 = 09:15:58.37 EST. While a time difference of 0.14 seconds may not seem significant, at this time β is increasing at about 8 degrees/second, and so 0.14 seconds can make a difference of over 1° in β , which can be significant in terms of loads on the tail.

²³ A sound spectrum analysis of the “loud bang,” performed by NTSB CVR specialists, indicates that the sound was transmitted from its source to the area microphone through air, and not through the structure of the airplane.

Another estimate of the time of tail separation can be obtained by examining the lateral load factor and heading data recorded on the FDR, and by comparing this data to simulations of the accident motion. Figure 3.2.1 compares the FDR heading²⁴ to the computed heading from the “NTSB Match v17” simulation, described in *Addendum 1*. At 09:15:58.3, both the simulation and FDR heading data are decreasing. At 09:15:58.5, the simulation heading has leveled out and thereafter increases, while the FDR heading decreases throughout. This different behavior is the result of the tail separating from the accident airplane, so that it is no longer able to provide the yawing moment that results in the reversal of the heading slope evident in the simulator data. The tail therefore must have separated sometime in the neighborhood of 09:15:58.4.

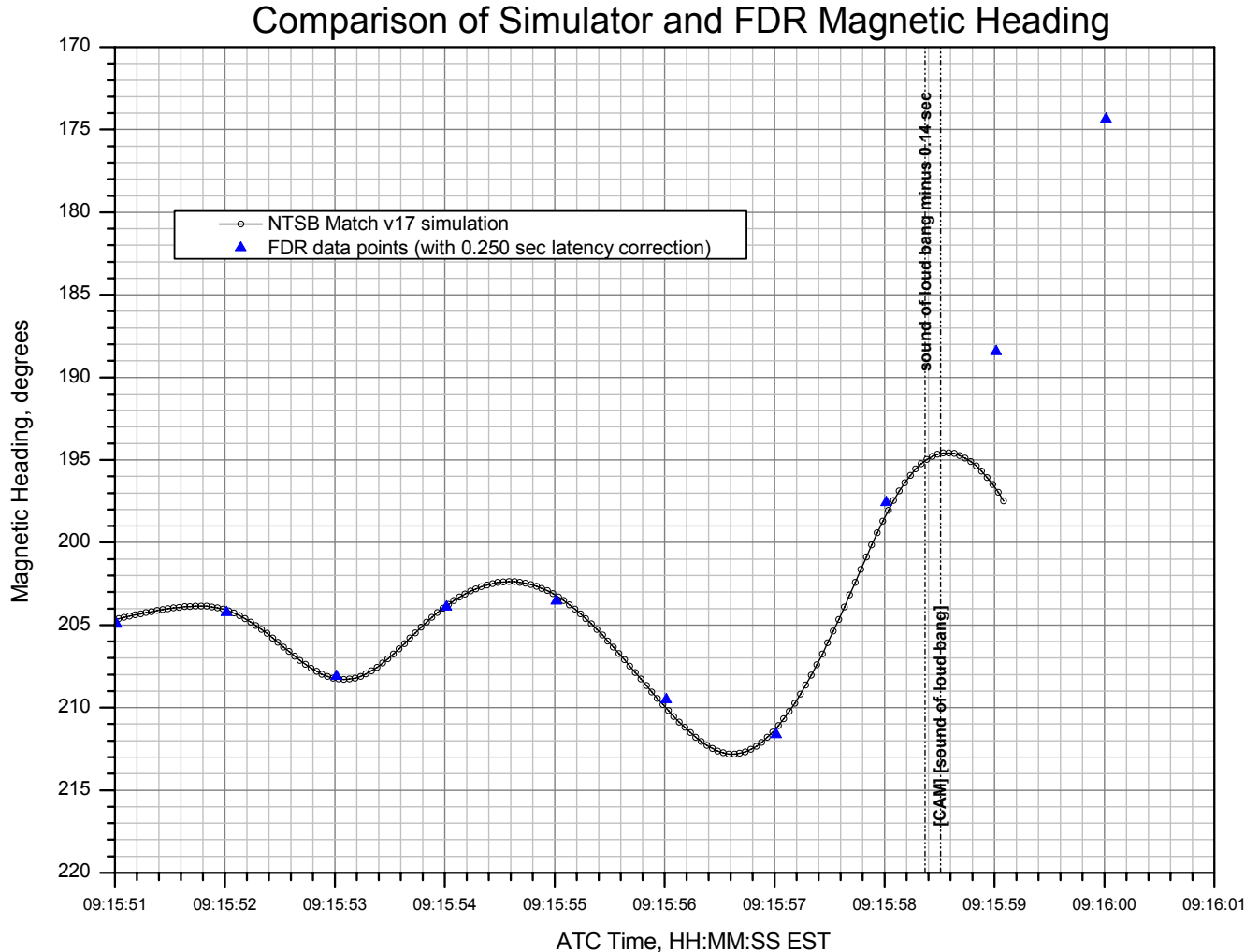


Figure 3.2.1.

Figure 3.2.2 compares the FDR lateral load factor (n_y) to the computed n_y from the “NTSB Match v17” simulation. The reversal in the slope of n_y in the simulator data corresponds to the reversal of the heading slope shown in Figure 3.2.1; because the FDR heading does not reverse, but continues decreasing, one would expect the FDR n_y trace to do the same. Figure 3.2.2 shows that, apart from the +0.2 g n_y jump between 09:15:58.45 and 09:15:58.95, the FDR n_y does indeed continue to decrease. The jump in n_y is consistent with the sudden removal of a side force to the left, which is the direction the vertical tail

²⁴ A latency of 250 ms on magnetic heading was assumed for the simulator match work (see *Addendum 1*).

would have been lifting when it separated. The n_y jump is therefore likely associated with the separation of the vertical tail.

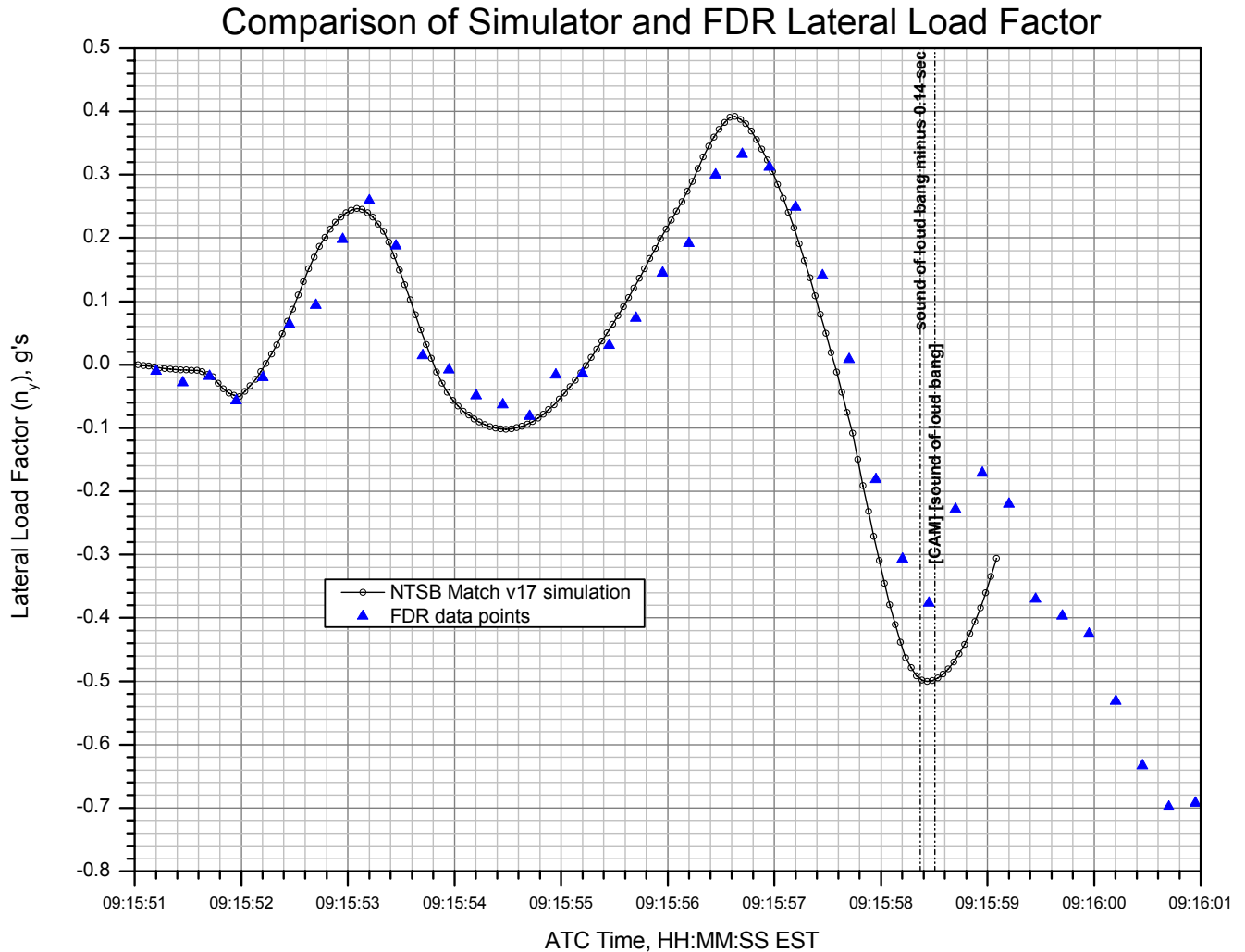


Figure 3.2.2.

Figure 3.2.3 shows the FDR n_y data at a larger scale around the time of the +0.2 g jump. Prior to the tail separation, the slope of the n_y data would be negative. Following the tail separation, the slope of the n_y data would be positive during the “jump,” after which it would again be negative as the heading continued to decrease (and the β increase). Examining Figure 3.2.3, this reversal of slope must have occurred between 09:15:58.20 and 09:15:58.45, which represent the last and first points defining known negative and positive slopes, respectively. Extending the negative and positive slopes that include these points as shown in Figure 3.2.3, the resulting intersection (at 09:15:58.40) provides a refined estimate of the time of tail separation. This is in good agreement with the estimate of 09:15:58.37 obtained above using the “sound of loud bang,” and so 09:15:58.37 is assumed for the time of tail separation in evaluating the loads.

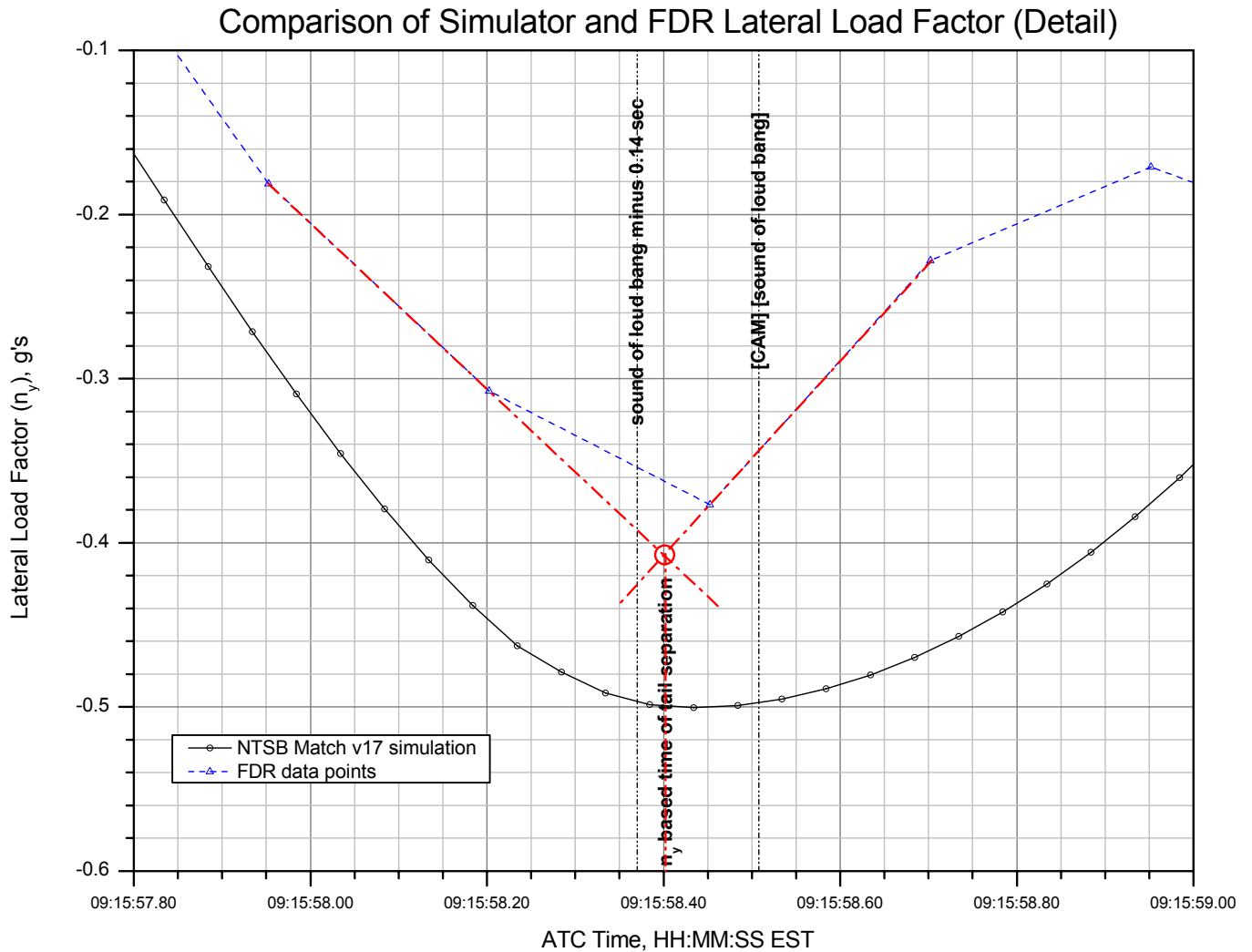


Figure 3.2.3.

Referring to Figure 2.4.1, at 09:15:58.37 β_{EFF} is between 12.3° and 13.6° , which are the boundaries of the calculation corresponding to the minimum and maximum values of the heading latency, respectively. If we include the $+0.5^\circ / -1^\circ$ uncertainty associated with the β calculation itself (as described in Section 3.1.2), then the possible range for β at the time of the lug fracture is 11.3° to 14.1° .

3.3. Rudder Angle Used for Loads Calculations

As described in the *Aircraft Performance Study*, data from the rudder position sensor is passed through a first-order lag filter before being recorded on the FDR, which removes frequency content from the data and distorts the original signal, so that the recorded rudder position does not match the position actually detected by the sensors. The *Study* presents two candidates for the actual rudder position: one based on a mathematical “inverse filtering” of a curve fit through the recorded rudder points, and another produced by Airbus based on an iterative solution that results in a good simulator match of the airplane motion as recorded by the FDR²⁵. These rudder positions are compared in Figure 3.3.1, which is a duplicate of Figure 29 in the *Study*.

²⁵ The Airbus rudder position calculation is described in Reference 5.

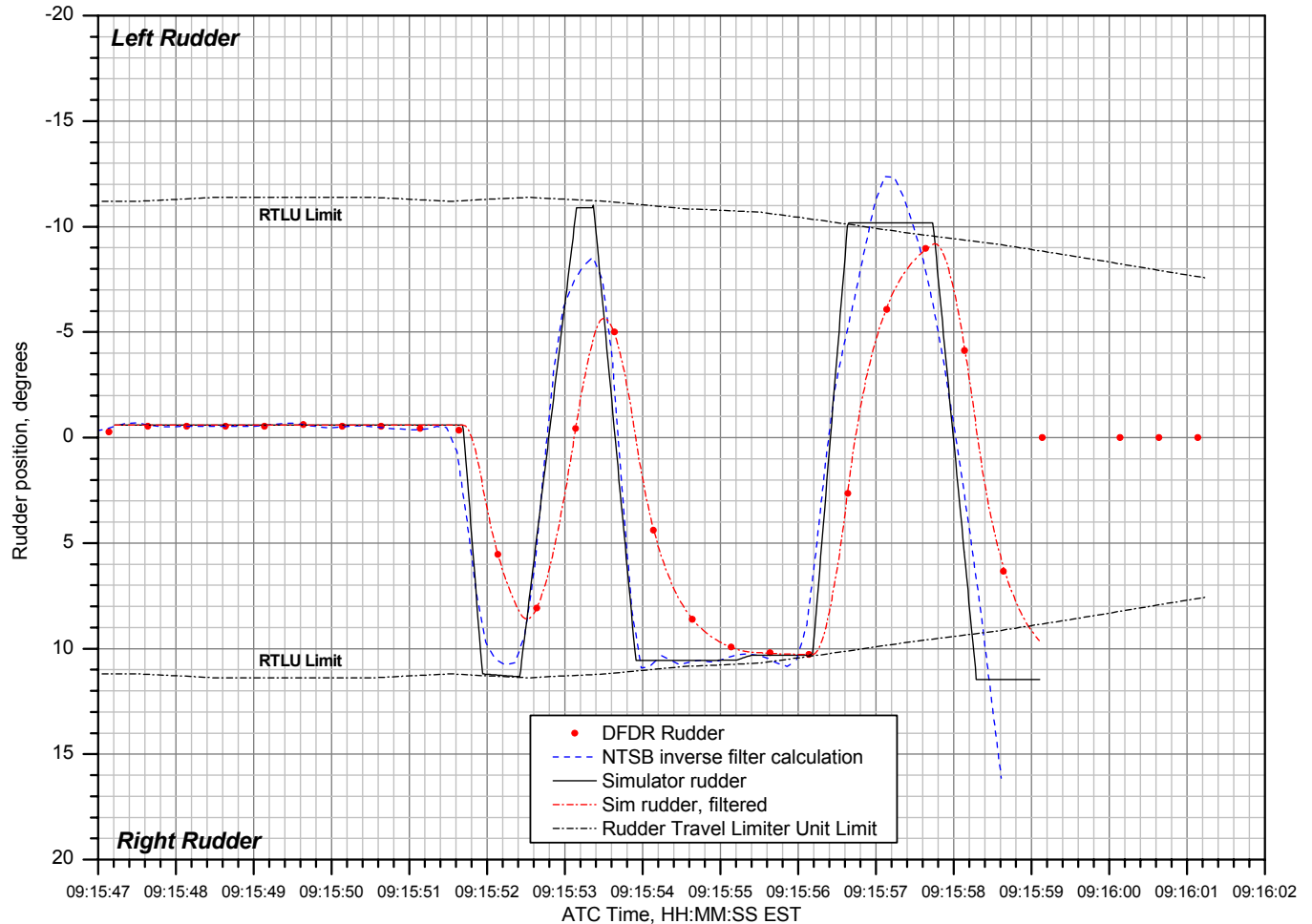


Figure 3.3.1. Comparison of the “inverse filter” rudder and the Airbus simulator rudder.

Both the “inverse filter” rudder and the Airbus simulator rudder satisfy the requirement that, when filtered, they produce signals that match the data recorded on the FDR. The Airbus rudder also satisfies rudder control system constraints imposed by the Rudder Travel Limiter Unit (RTLUL) and the relationships between the rudder position, pedal position, and yaw damper operation (see Reference 5). While both rudder estimates exceed the nominal limits of the RTLUL near the end of the data in Figure 3.3.1 in order to match the recorded FDR data when filtered, the Airbus rudder stays closer to the RTLUL limits, and is more consistent with the pedal being held at the pedal stop during these times. Furthermore, the Airbus rudder has a square-wave shape that is more consistent with the stop-to-stop pedal inputs recorded on the FDR²⁶. For these reasons, the Airbus rudder is used in the NTSB simulations described in *Addendum 1* to the *Study*, and here in the estimates on the loads on the tail.

Note in Figure 3.3.1 that the Simulator rudder deflects to 11.5° right prior to 09:15:58.37, the moment of the vertical tail right rear lug rupture. This deflection is required to match the recorded FDR rudder point at about 09:15:58.6, which is recorded after the time of the

²⁶ The low sample rate of the pedal position data recorded on the FDR prevents the shape of the pedal inputs from being defined with absolute certainty and precision. However, given the high rate of pedal input apparent in the data, and the location of pedal data points at or beyond the pedal stops (indicating cable stretch), a square-wave type input on the pedals is more likely than the smooth, continuous inputs suggested by the inverse-filter solution for rudder.

rupture, and is 1.3° greater than the 10.2° left value corresponding to the previous rudder swing, where the rudder is at the RTLU limit. However, it is possible that the rudder was at the RTLU limit up to the point of rupture, and then started to move beyond the RTLU limit after the rupture, accounting for the FDR data point at 09:15:58.6. Consequently, this point can not be used to determine the rudder position at rupture; instead, the position must be estimated based on the constraints imposed by the RTLU, starting from the previous rudder position at 10.2° left. During the swing from left to right, the RTLU will act to close the rudder limit by about 0.4° ²⁷, putting the new limit at about 9.8° . Work done by Airbus²⁸ indicates that at the high load condition at this point, structural flexibility can produce inputs to the rudder actuators that would move the rudder an additional 0.6° beyond the rigid tail value; this could account for a rudder at approximately 10.4° prior to separation. In addition, high pedal forces can produce some additional small rudder deflections (about 0.2°) by physically distorting the RTLU mechanism. Given the uncertainties involved with the actual RTLU closure rate, the effects of structural flexibility, and the distortion of the RTLU mechanism due to high pedal forces, the rudder angle at rupture is estimated to be between 10° and 11° . The low sampling rate of the rudder data, combined with the effects of the SDAC filter, prevent the FDR data from resolving the rudder position at rupture any further, and so the question is treated here as an uncertainty in the rudder angle which contributes to the overall uncertainty in the loads calculation. The results of this approach are shown in Section 3.5.

3.4 CFD Results

A converged, steady state CFD solution was reached within 2000 iterations for the rigid cases at all conditions. For the cases with aeroelasticity included, the lower sideslip angles converged in 2000 iterations, and the sideslip cases larger than -10 degrees converged in 3000 iterations.

Integrated coefficients and surface pressure were calculated for both the rigid and flexible grid cases. Solutions were determined at both wind tunnel and at accident conditions. The integrated coefficients and the determination of the loads are described in the next section.

3.4.1. CFD Results for Wind Tunnel Conditions

Surface pressure distributions calculated with the CFD code at the same freestream conditions as the wind tunnel data for the A330-200 rigid model were provided by Airbus. A data sample was provided at 900 points on each side of the fin, and consisted of data at the same spanwise locations as the pressure measurement locations on the wind tunnel data for a direct comparison of the pressure distributions. Aerodynamic coefficients of interest were obtained by integrating the pressures calculated at each cell in the computation, over the entire surface of the fin, accounting for local curvature.

²⁷ This assumes the RTLU motor is running at its full speed of 0.7 degrees/second. The actual performance of the RTLU in these circumstances – including its start-up time and acceleration – are undetermined, and so the actual closure of the RTLU during the final rudder swing may be less than 0.4° .

²⁸ See Reference 12.

A comparison of the CFD surface pressure distribution and the surface pressures measured in the wind tunnel tests was performed to check the accuracy of the CFD solution. Whereas several millions of nodal points were calculated in the CFD solution, a subset of fin surface points were used to minimize the size of the data files, yet still capture the salient features of the flow. However, the computational grid used in the CFD code were not regularly spaced along the fin. To facilitate the comparison, the CFD data was imported into the MATLAB commercial code, and utilizing a three dimensional triangle based cubic interpolation, the data was arranged to a regularly space grid. Once in MATLAB, the data was more readily examined, and surface pressures were easily compared to the available wind tunnel results.

Figures 3.4.1 and 3.4.2 show chordwise pressure differential distributions at four spanwise locations, denoted non-dimensionally by η . In these Figures, the wind tunnel data has been interpolated to allow easier comparison with the CFD solution. Results are shown in the Figures for β of -8° and -10° , the sideslip angles where the nonlinearities start to appear in the coefficients. At -8° , the CFD captures most of the features in the wind tunnel data, including the location and value of the pressure peak near the leading edge, and the reduction of the pressure peak near the tip of the fin. The small peak that exists near the rudder gap is also captured by the CFD solution, as well as flow separation over the rudder, as evident by the flattening of the rudder gap peak near the tip. As mentioned in previous sections, the quantitative over-prediction of the load by the CFD is evident in the distributions. However, the trends shown in the wind tunnel data are accurately reproduced.

A similar comparison is shown in Figure 3.4.2 for sideslip of -10 degrees. Here, a favorable comparison of the trends in the data is evident for the features of the distribution as discussed above. However, the CFD shows a consistent overprediction of the pressure peak near the leading edge of the fin. The wind tunnel pressure distributions show features consistent with a larger area of flow separation than that indicated by the CFD pressure distribution, which explains why the CFD loads are greater than the wind tunnel loads.

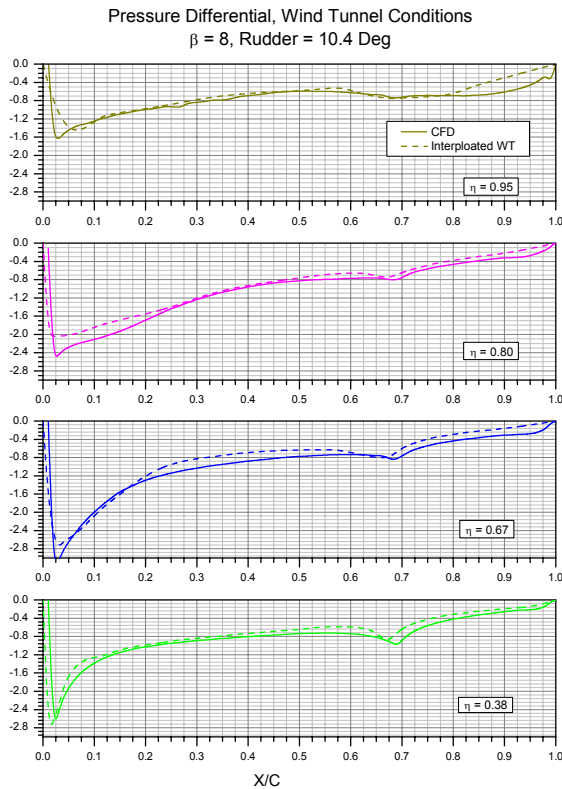


Figure 3.4.1.

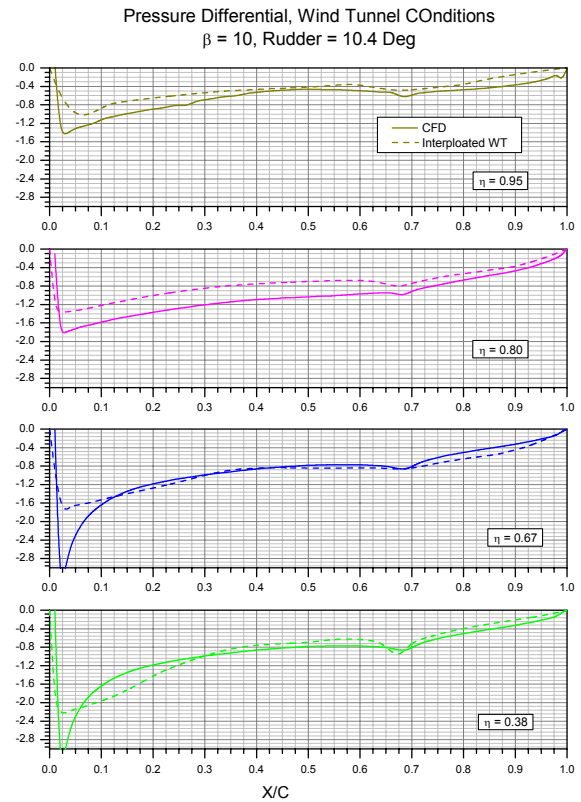


Figure 3.4.2.

The pressure distributions shown above also show indications of a spanwise progression of a separated flow area in the wind tunnel data. To examine how the CFD solution captured the spanwise pressure gradient, a numerical integration of the chordwise pressure distributions was performed at the spanwise locations where wind tunnel data existed. Figure 3.4.3 shows the spanwise distribution of the integrated pressure distributions for sideslip angles between -4° and -10° . All are shown on the same scale.

For all of the sideslip angles, the integrated pressures show the over-prediction mentioned in the previous sections. However, the shape of the distribution, particularly at the lower sideslip angles, show similarity. The relative reduction of integrated pressure near the tip of the fin is close to the same reduction seen in the CFD data for all but the highest sideslip angles. At $\beta = -10^\circ$, the CFD results do not capture the same extent of the separated region as evident in the wind tunnel data, yet the trends are similar. The similarity of the pressure distributions and the onset of flow separation provided confidence that the CFD solution was capturing most of the important features of the flow. As expected with computational results, the greater the level and extent of separated flow, the less the accuracy of the calculated solution.

The overestimation of the pressures on the low pressure side of the fin could be attributed to several of the factors cited previously, such as boundary layer tripping modeling, grid enhancements, and trailing edge estimations. Some of these factors were investigated in further studies. These studies found that a further refinement of the grid size near the trailing edge of the rudder provided a slight reduction in predicted coefficients. Additionally, the gap between the rudder and the fuselage at the base of the fin was modeled in this study as a continuous piece that, with the rudder deflected, extended down to the fuselage, adding to the total area of the fin and rudder. Later studies with the proper modeling with a

gap between the rudder and fuselage allowing a slight flow relaxation around the trailing edge provided further reduction of the coefficients (7.5% reduction in shear load coefficient, 4.5% reduction in bending moment coefficient, and 4.1% reduction in torsion coefficient). The examination of the pressure distributions demonstrated the capability of the CFD solution to adequately capture the onset and development of the separated flow.

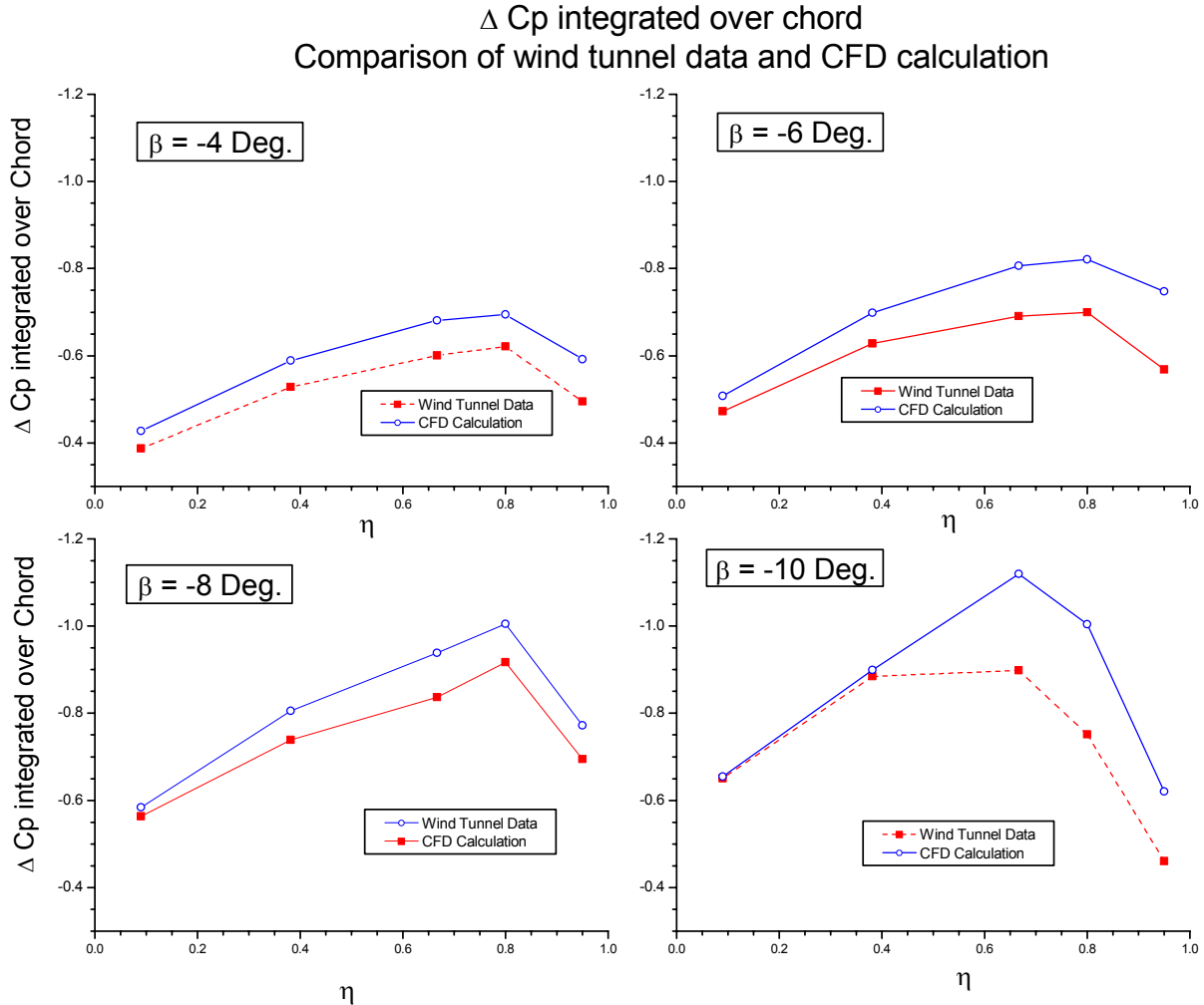


Figure 3.4.3.

3.4.2. CFD Results for the Rigid, Full Scale Configuration at Accident Conditions

Surface pressure distributions were calculated with the CFD code on each side of the fin. These pressure distributions were used to examine the extent and relative magnitude of the flow separation at the flight condition. Shown in Figure 3.2.4 are examples of two such calculations on the suction (low pressure) side of the rigid fin at accident conditions, rudder angle of 11.5° , and at two airplane sideslip angles of -6° and -13° . At the lower sideslip angle, the solution shows an attached flow, with a large low pressure peak near the leading edge which quickly tapers towards the trailing edge. At -13° , the low pressure peak has been drastically reduced towards the tip of the fin, yet the inner portion of the fin still generates a large low pressure peak. Also note that separation also appears over the deflected rudder.

As seen in the integrated coefficient data β -polar, the bending moment had the largest non-linearity appear at the higher sideslip angles. Inspection of the loading produced by the pressure distributions shows that flow separation occurs predominantly near the tip of the fin, yet the lower half of the fin continues to generate a large low pressure peak. Examining the bending moment shows that the net effect of the tip separation tends to change the center of pressure for bending moment action towards the base of the fin. Hence as sideslip angle increases, the increased side force generated by the lower portion of the fin acts at a point that moves towards the base of the fin, leading to a greater non-linearity in the bending moment than the side force. The change in point of action also acts to introduce nonlinearity to the torsion coefficient.

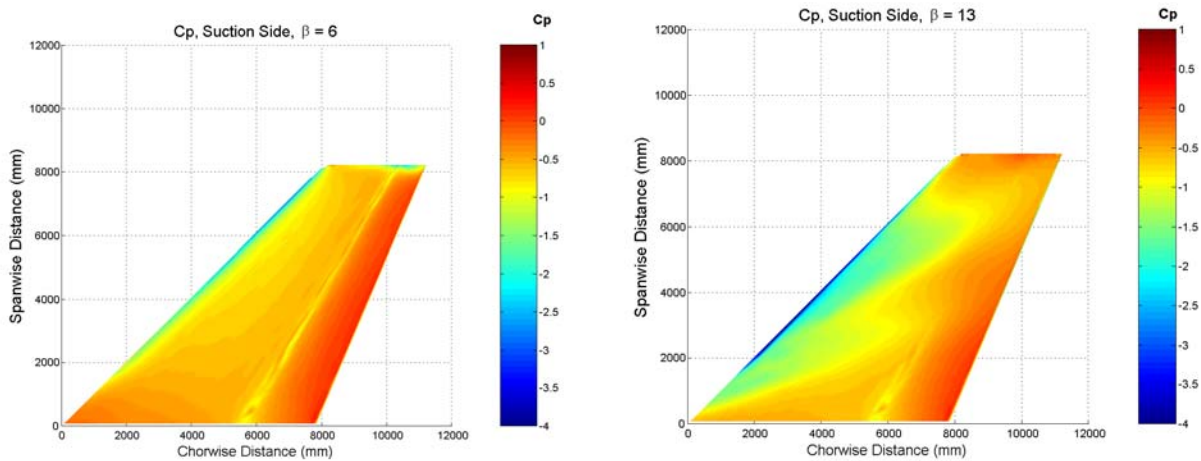


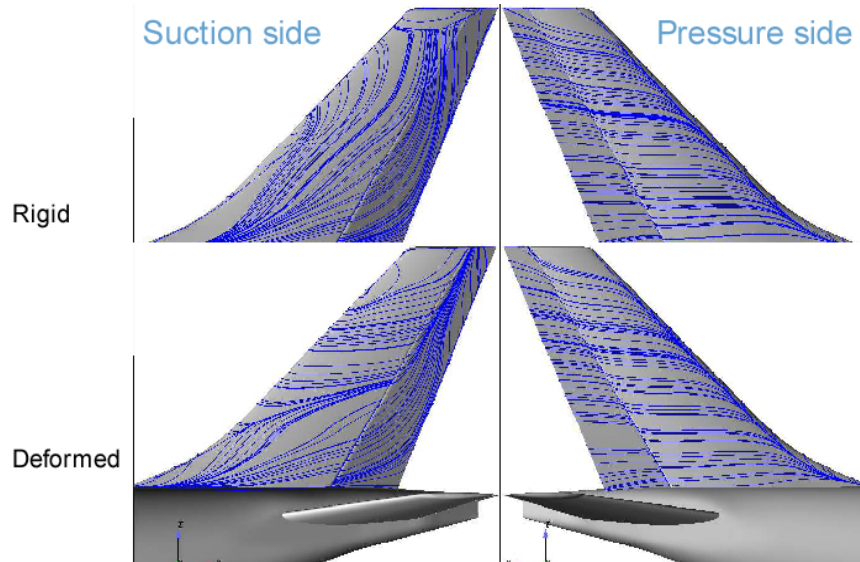
Figure 3.2.4. CFD pressure distributions, Accident Conditions, rigid aircraft.

Flexible, Full Scale Configuration

Airbus studied the aerodynamic characteristics of the flexible structure using the NASTRAN/Truckenbrodt method and TAU code as described in Section 1.5. The resulting deformed geometry showed a local reduction of sideslip angle on the vertical tail due to fuselage and tail bending. The reduction in local sideslip angle had the tendency to reduce the overall loading slightly due to the lower local incidence angle. However, this also led to a reduction in the level of flow separation on the tail, leading to less non-linear behavior than evident in the wind tunnel data and the calculations for the rigid aircraft. An example of the results demonstrating this is shown in Figure 3.4.5, comparing the computed surface streamlines for the full scale rigid and flexible results at airplane sideslip of 12° . On the low pressure side, the level of flow separation, as indicated by the more orderly chordwise flow, is considerably less for the flexible configuration than the rigid calculations.

An additional set of calculations for the flexible, full scale configuration was provided by Airbus for the same conditions, yet with a rudder deflection of 10° . The second diagram in Figure 3.4.5 shows the surface streamlines for the rudder = 10° calculation. Comparison with the 11.5° rudder result shows a similar level of flow separation on the rudder itself on the low pressure suction side of the fin, but a lower level of flow separation on the fin. The reduction in flow separation is denoted by the reduction in crossflow, i.e. the flow moving towards the tip of the fin. The deformed results show a further reduction of separated flow, similar to the rudder = 11.5° results.

$\beta = -12^\circ$, Rudder = 11.5° , Accident conditions



$\beta = -12$, Rudder = 10 , Accident conditions

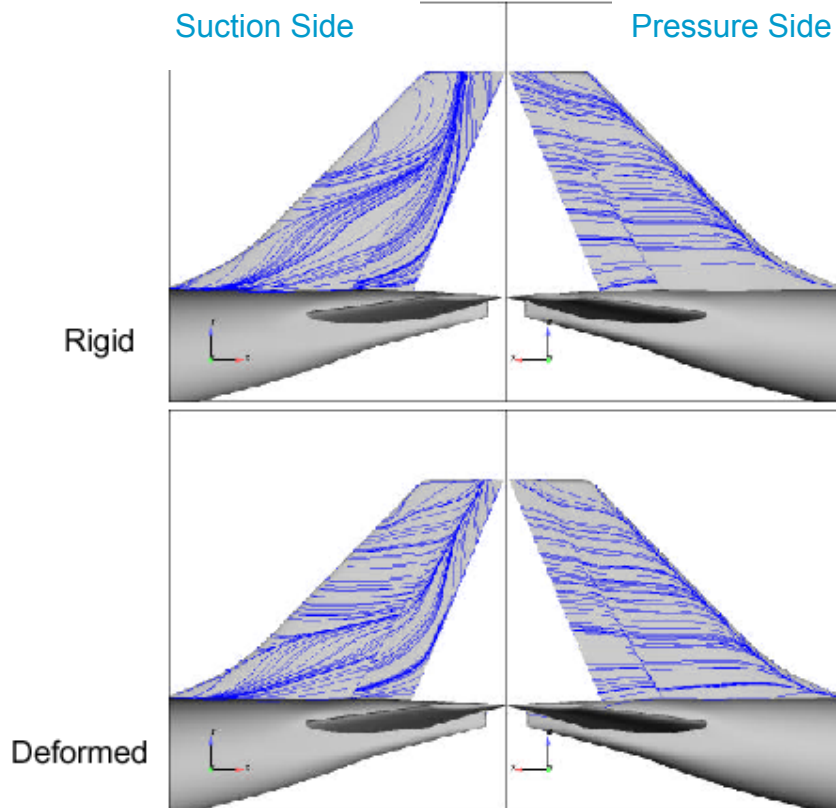


Figure 3.4.5. Flow streamlines for the rigid and deformed tail at 12 degrees of sideslip, rudder at 11.5° and 10° .

A comparison of the integrated CFD load coefficient results for the rigid and flexible configurations is shown in Figure 3.4.6. The effect of localized reduction in sideslip angle for the flexible configuration is clearly evident with the overall reduction in all coefficients, more predominant at the higher sideslip angles. The reduction of the non-linear effect is most noticeable in the bending moment coefficient, where the onset of the nonlinearities is delayed to higher sideslip angles.

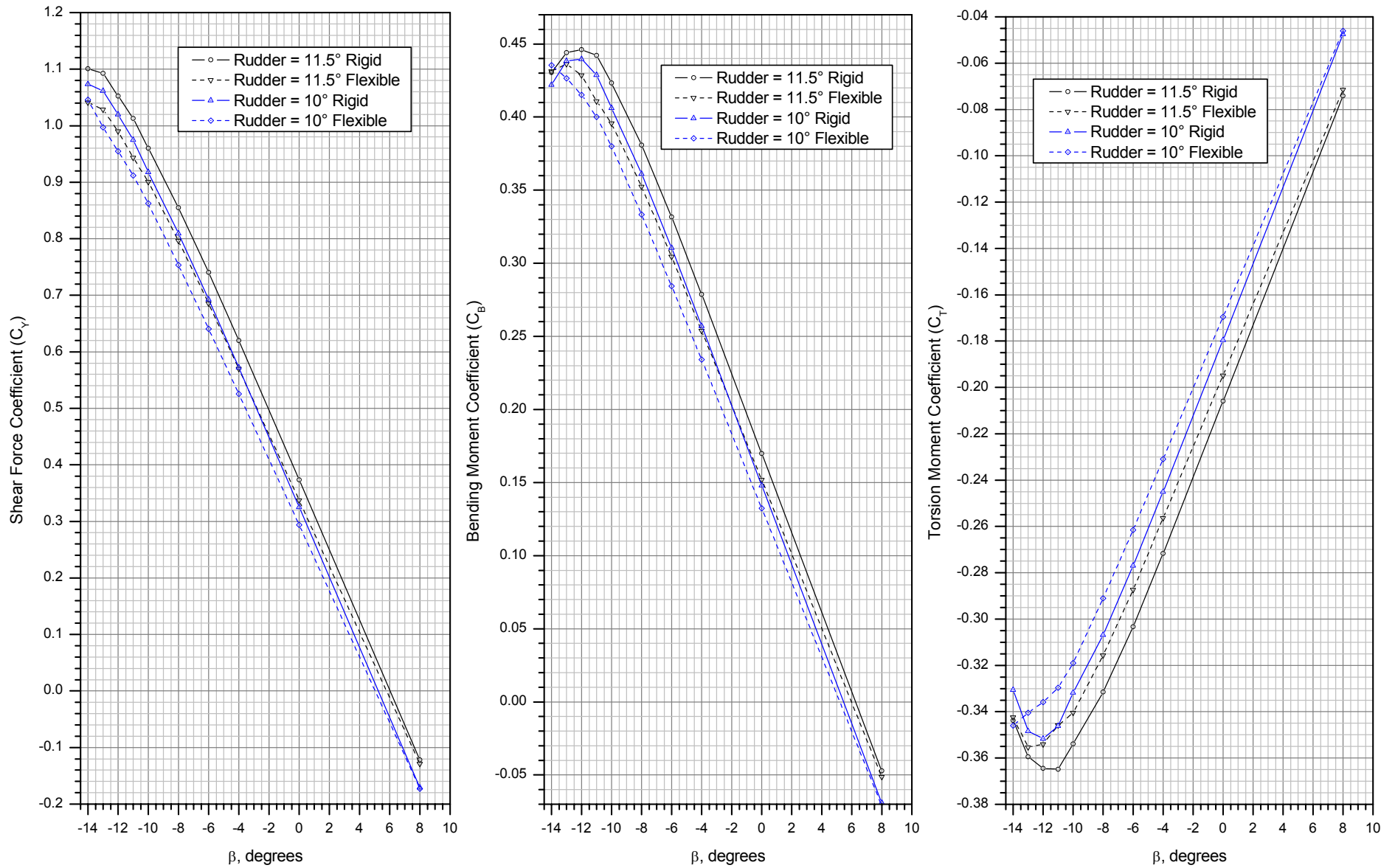


Figure 3.4.6. Comparison of rigid and flexible vertical tail load coefficients.

3.5. Load Ranges at Time of Vertical Tail Separation

3.5.1. Method 1 Loads at Rudder = 10° and 11°

The shear force, bending moment, and torsional moment coefficients at $\delta_r = 10^\circ$ and 11° resulting from Method 1 are presented in Figure 3.5.1. The loads predicted by the LLM (including flexibility effects) are provided for comparison. The differences between the Method 1 solution and the LLM in the linear region are due to the following:

- The CFD correction factor is selected so as to force the Configuration 3 data in Table 1 to match the Configuration 2 data, and the Configuration 2 data does not match the LLM perfectly (cf. Figure 2.1.1).
- Method 1 includes wind tunnel to flight condition corrections, and the LLM does not.
- There is an inherent uncertainty of about 5% of the maximum wind tunnel load in the wind tunnel data, and the LLM and Method 1 curves are based on two different wind tunnel tests. This uncertainty is greater than the differences between Method 1 and the LLM shown in Figure 3.5.1.
- There are small differences in the flexibility effects computed by the CFD/FEA method and those inherent in the LLM module.

The “Method 1 calculation” curve at $\delta_r = 11^\circ$ is used to evaluate the Method 1 loads in the β range in which the tail separated from the airplane, as described below.

Final CFD-Based Load Coefficients: Method 1

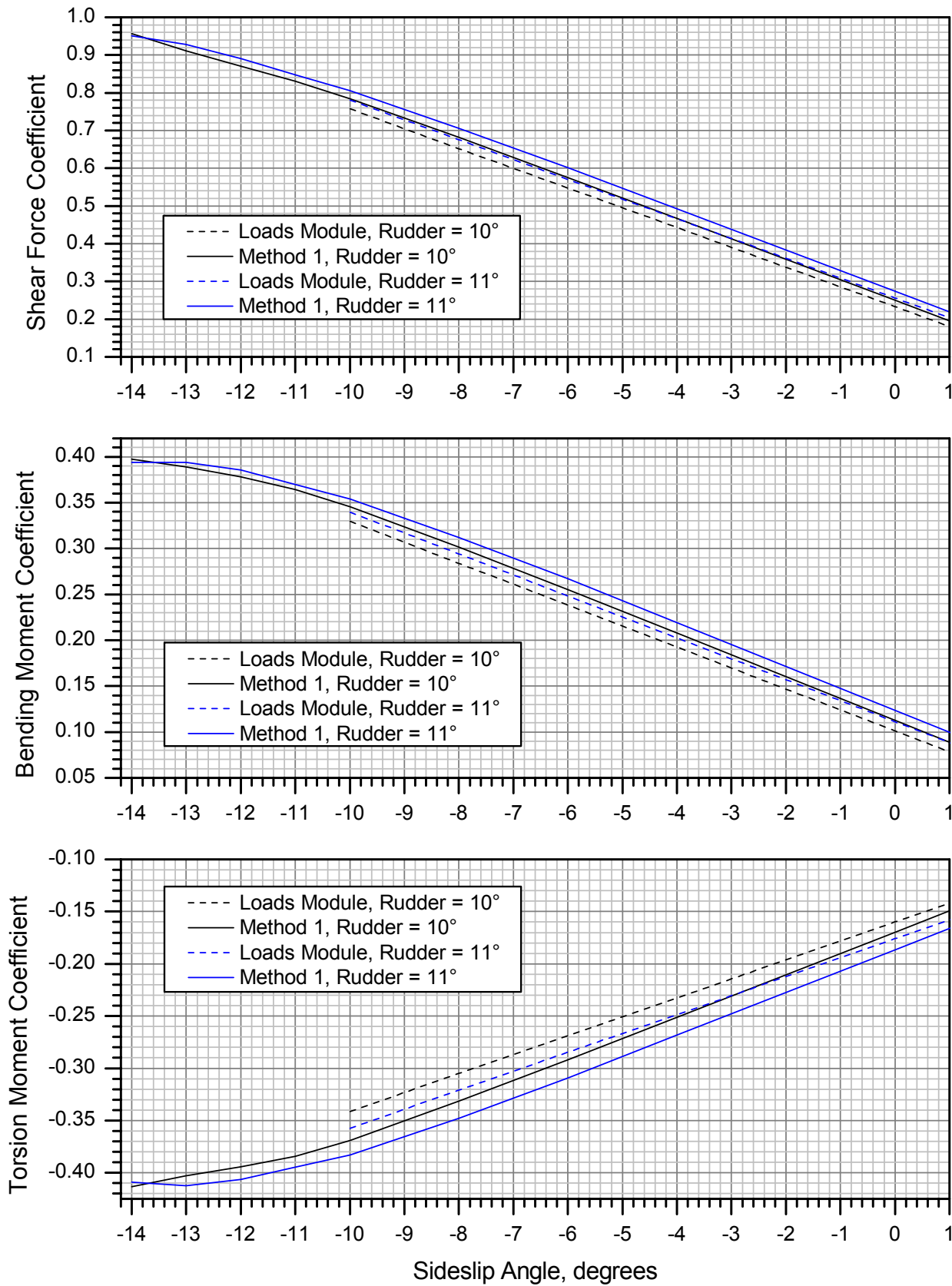


Figure 3.5.1.

3.5.2. Method 2 Loads at Rudder = 10° and 11°

The shear force, bending moment, and torsional moment coefficients for $\delta_r = 10^\circ$ and 11° resulting from Method 2 are presented in Figure 3.5.2. The loads predicted by the LLM (including flexibility effects) are provided for comparison.

The “Method 2” solution in the bending moment plot of Figure 3.5.2 is the result of the calculations described in Section 2.3, with a small, manual adjustment between $\beta = -11$ and $\beta = -13$. The unadjusted result has a peak at $\beta = -11^\circ$, beyond which the loads start to decrease. This is not consistent with the flexible CFD predictions of the bending moment behavior in the non-linear region (see Figure 3.5.1) or with other wind tunnel data evidence²⁹. Accordingly, the result in this area was manually adjusted to remove the peak, giving the result shown in Figure 3.5.2. The adjustment was made to keep the data consistent with the expected behavior of the bending moment, and to provide a conservative “lower bound” for the bending moment estimate; the Method 2 loads are consistently lower than the “Method 1” results, so the two Methods in combination bracket the possible range of loads and the difference between the two methods represents much of the uncertainty in the loads estimates. This uncertainty is discussed further in Section 3.5.3.

The Method 2 solution better matches the LLM in shear and bending moment because the Configuration 2 data, which is the baseline for Method 2, is adjusted to match the LLM in the linear region. The small differences in shear and bending moment are due to the wind tunnel to flight increments predicted by CFD and small differences in flexibility effects between the CFD/FEM solution and the LLM.

The “Method 2” curves at $\delta_r = 10^\circ$ are used to evaluate the Method 2 loads in the β range in which the tail separated from the airplane.

²⁹ Data from another wind tunnel test of an A330 model in different flight conditions indicates that the side force contribution of the horizontal and vertical tails to the total side force on the airplane tends to remain relatively constant in the non-linear region and does not decrease, even out to $\beta = 30^\circ$. This data provides a sense of the behavior of the loads but can not be used to determine the absolute value of the loads on the vertical tail alone, because it includes the effects of the horizontal tails, and only measures total side force on the airplane, not the pressure distribution over the vertical tail, which is required to resolve the bending and torsion moments.

Final CFD-Based Load Coefficients: Method 2

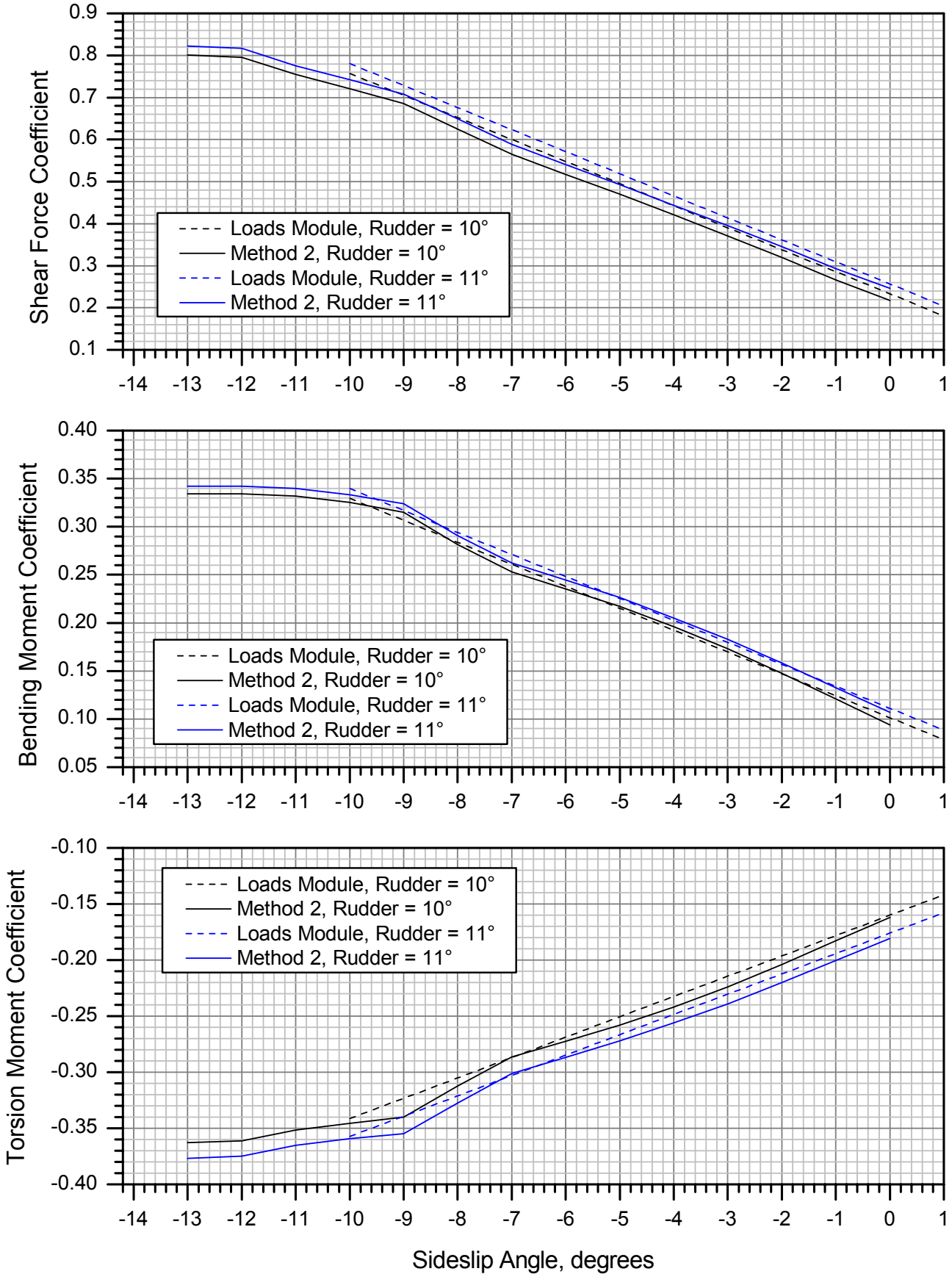


Figure 3.5.2.

3.5.3. Load Ranges at Time of Vertical Tail Separation

The loads at the time of the vertical tail separation, in the vertical tail axis system, are calculated by using β at the time of separation to look up the C_Y , C_B , and C_T coefficients in the airplane axis system, solving Equations [2] for Y, B, and T with \bar{q} for the time of separation (212 lb/ft² at 09:15:58.37 EST), and then transforming the results into the vertical tail axis system using Equation [13]. As discussed above, there is a range of possible β at 09:15:58.37, and also a range of possible loads at a given β . These ranges define the uncertainty in β and loads at the time of separation, and define an uncertainty “box” if the load range is plotted as a function of the β range, as shown in Figures 3.5.3 (a), (b), and (c).

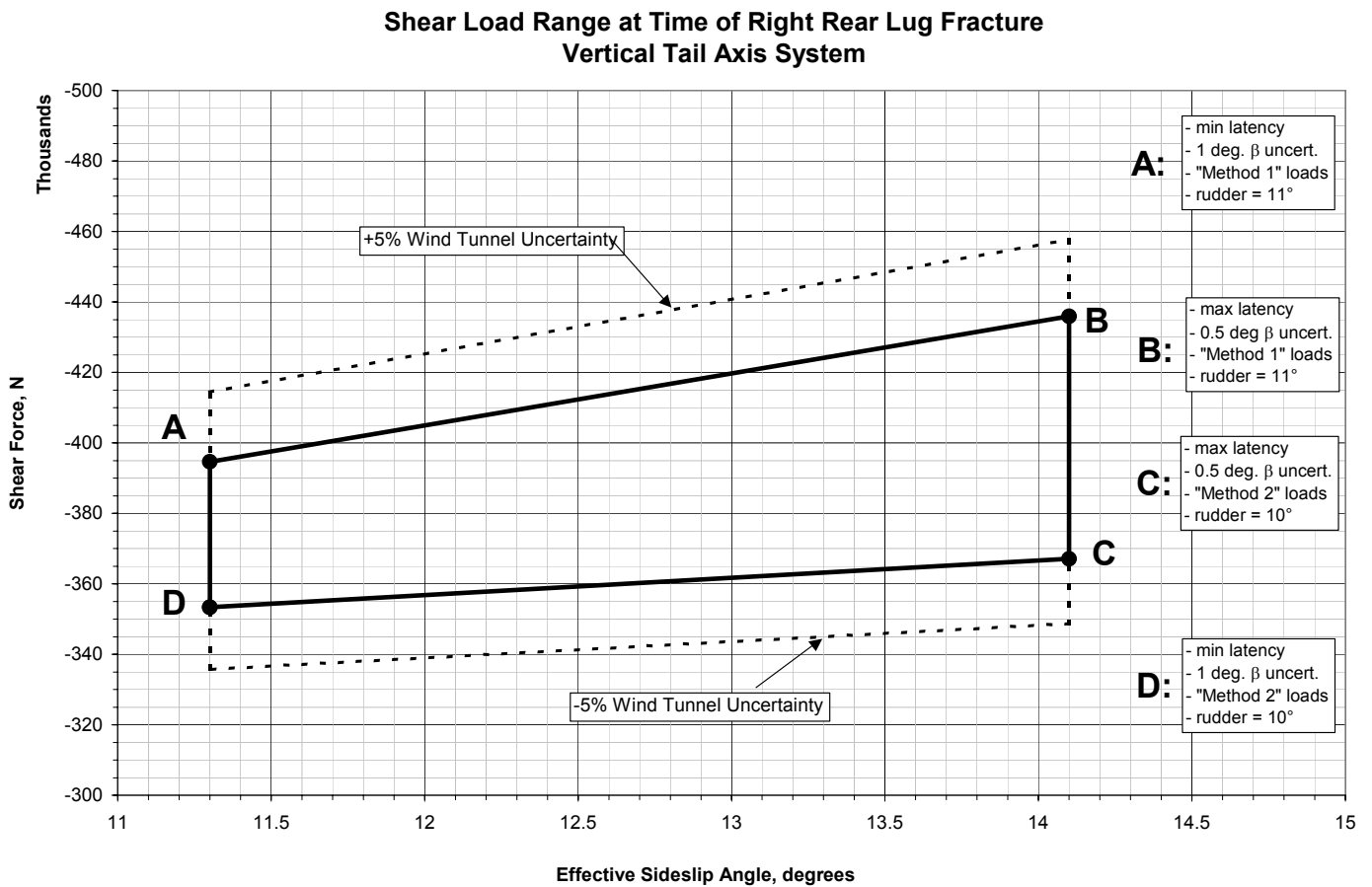
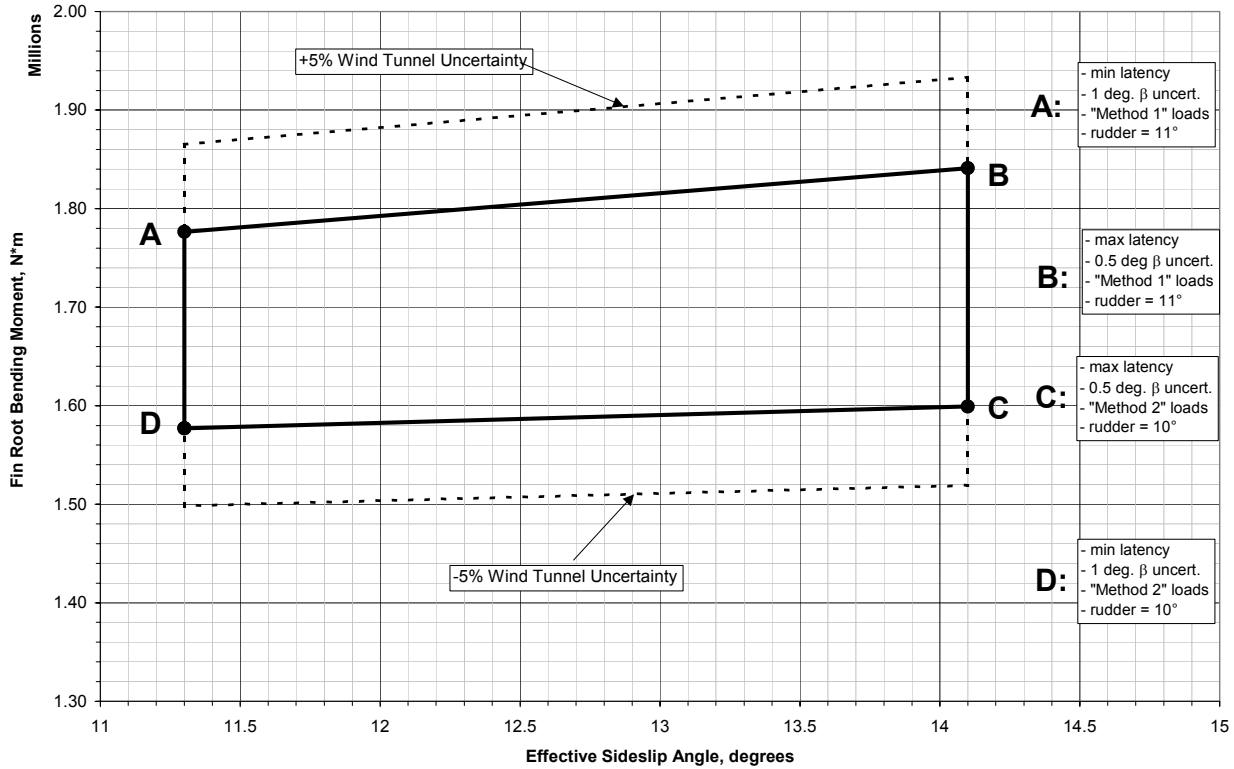
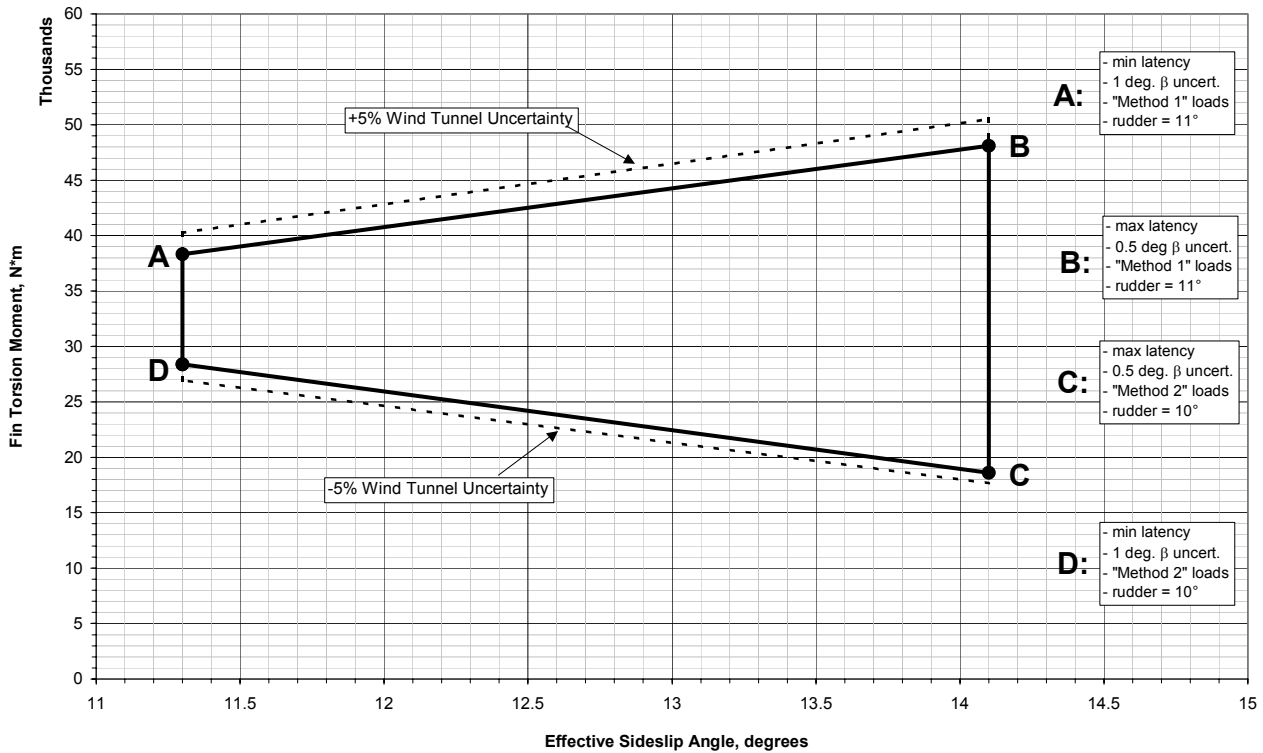


Figure 3.5.3 (a).

**Bending Load Range at Time of Right Rear Lug Fracture
Vertical Tail Axis System**



**Torsion Load Range at Time of Right Rear Lug Fracture
Vertical Tail Axis System**



Figures 3.5.3 (b) and (c).

The corners of the heavy lines drawn in Figures 3.5.3 represent the bounds of the β and loads ranges resulting from the uncertainty in the β and loads calculations. The thin dashed lines above and below the heavy lines represent an additional uncertainty equal to 5% of maximum loads, in order to account for the experimental uncertainty inherent in the A330 wind tunnel data upon which both Method 1 and Method 2 are based.

Figures 3.5.3 indicate that the possible range in loads at the time of tail separation, including all uncertainties, are as follows:

Shear Force: $-353,000$ to $-436,000 \pm 5\%$ N
Bending Moment: $1,580,000$ to $1,840,000 \pm 5\%$ N*m
Torsion Moment: $-18,600$ to $-48,100 \pm 5\%$ N*m

The loads in the vertical tail axis system can be used to compare the loading on the tail at the time of separation to the tail's design load envelope. Figures 3.5.4 (a) and (b) are "correlated shear force diagrams" prepared by the Structures Group Chairman. The points labeled "Corner A," "Corner B," etc. in Figures 3.5.4 correspond to the same corners shown in Figures 3.5.3. Figures 3.5.4 indicate that the loads at the time of tail separation are well outside the ultimate load design envelope.

Daniel R. Bower, Ph.D.
Senior Aerospace Engineer

John O'Callaghan
National Resource Specialist – Aircraft Performance

CORRELATED SHEAR FORCE DIAGRAM A300-600R

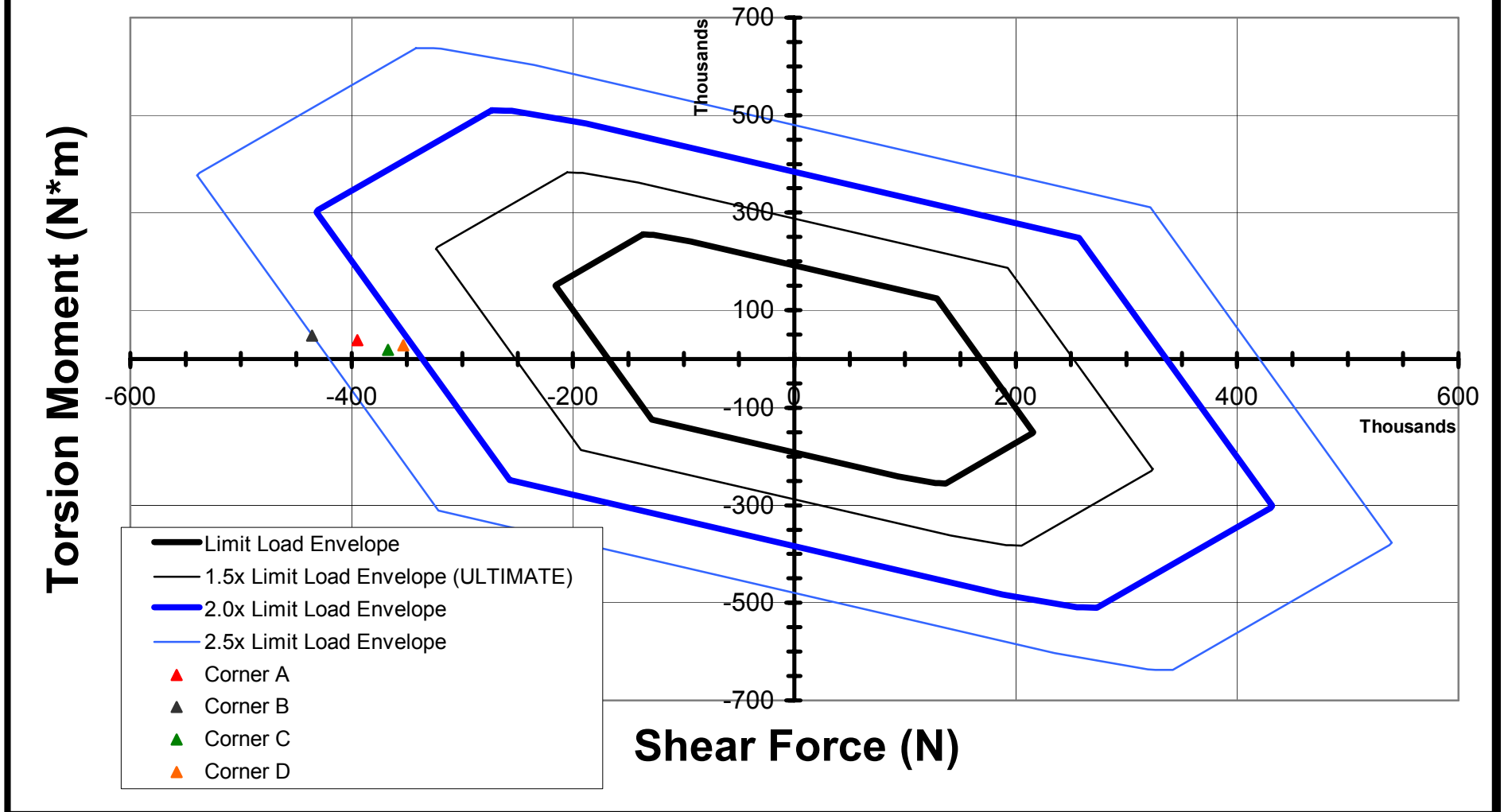


Figure 3.5.4 (a).

CORRELATED SHEAR FORCE DIAGRAM A300-600R

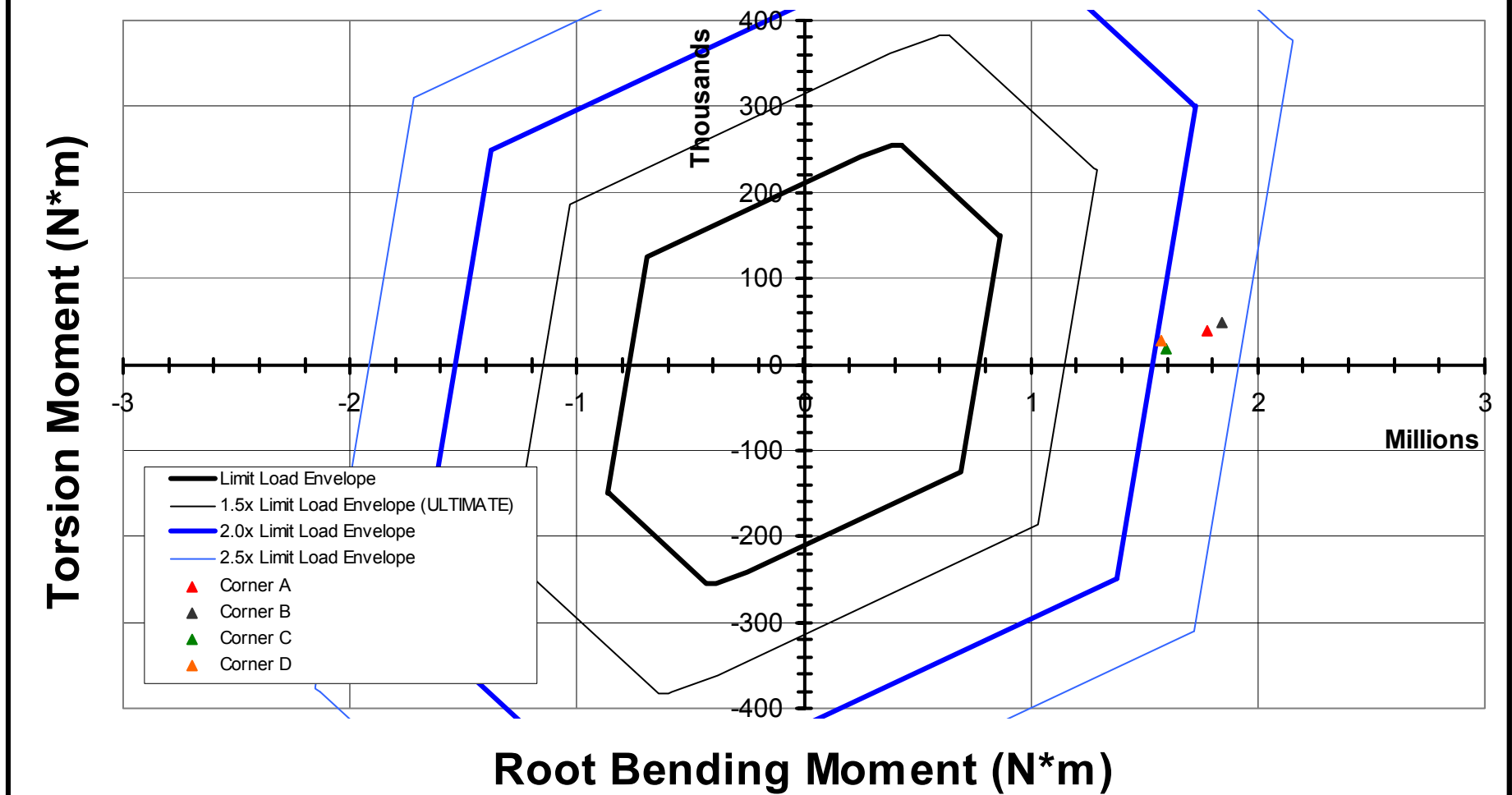


Figure 3.5.4 (b).

REFERENCES

1. National Transportation Safety Board, *Aircraft Performance Group Chairman's Aircraft Performance Study for American Airlines Flight 587 (DCA02MA001)*, October 10, 2002.
2. National Transportation Safety Board, *Addendum # 1 to the Aircraft Performance Group Chairman's Aircraft Performance Study for American Airlines Flight 587 (DCA02MA001)*, October 1, 2003.
3. Airbus memorandum EGAG-214/03, *Static pressures on the A330-200 fin: Results obtained from tests with the model 414D in ARA, test series C103/7*, March 17, 2003.
4. Gerhold, T., Friedrich, O., Evans, J., Galle, M., *Calculation of Complex Three-Dimensional Configurations Employing the DLR-TAU-Code*, AIAA-paper 97-0167, 1997. See also a description of DLR-TAU at http://www.taurus.dlr.de/user_guide/user_guide.html.
5. Airbus Technical Note 517.0082/2002, 2nd Edition, *AAL587 – Handling Qualities Investigations*, March 11, 2002.
6. Airbus Technical Note 517.0358/2002, 2nd Edition, *AAL587 Accident investigation: side-slip computation with integration method*, September 24, 2002.
7. H. Akima, *A New Method of Interpolation and Smooth Curve Fitting Based on Local Procedures*, Journal of the ACM, 17(4):589-602, October 1970.
8. Airbus presentation to NTSB ref. EGAG-746/03, *Investigation of flexibility effects on aero. data for loads on the VTP*, December 2003.
9. Dods, J. B. Jr., *Wind Tunnel Investigation of Horizontal Tails III – Unswept and 35° Swept-Back Plan Forms of Aspect Ratio 6*, NACA RM A8H30, 1948.
10. Dods, J. B. Jr., *Wind Tunnel Investigation of Horizontal Tails V – 45° Swept-Back Plan Form of Aspect Ratio 2*, NACA RM A9D05, 1949.
11. Colbe, C.D., Bandetti, A., *Investigation in the Ames 12-foot Pressure Wind Tunnel of a Model Horizontal Tail of Aspect Ratio 3 and Taper Ratio 0.5 Having Quarter-Chord Line Swept Back 45°*, NACA RM A51D02, 1951.
12. Airbus Technical Note # TN-ESGC-1023/04, *AA587 Airbus Structure Investigation: Rudder Mechanical Flight Control System Behavior under VTP deformation*, March 19, 2004.